Numerical Modelling of Integral Abutment Bridges

by

ABIOLA A. ODEJAYI

Submitted in Partial Fulfillment of The Requirements for The Degree of

Master of Applied Science

at

Dalhousie University

Halifax, Nova Scotia

October 2021

Dalhousie University is located in Mi'kma'ki,
the ancestral and unceded territory of the Mi'kmaq.
We are all Treaty people.

Table of Contents

List of Tables

List of Figures

ABSTRACT

Integral Abutment Bridges (IABs) are well known for their lower construction and maintenance costs by eliminating expansion joints and bearings. The flexible piles supporting the end-span abutments offer the possibility of this expansion and contraction of the superstructure caused by the daily and seasonal changes in temperature. This thesis focuses on achieving integral bridge abutments' long-term performance by evaluating available backfill alternatives. Field results from a monitored integral abutment bridge in Fredericton, New Brunswick, were firstly used to simulate the non-linearity of backfill soils using two finite elements soil models (Mohr-Coulomb and Hardening Soil). The magnitude of lateral earth pressure from different backfill options was then estimated using the validated Hardening soil model. Further study reveals that this magnitude of lateral earth pressure increases with time, and it significantly depends on the stiffness property of the backfill material. As a result, it is suggested to be the first consideration in the design, as its maximum constant value is essential for the behaviour of integral bridge abutments.

ACKNOWLEDGEMENTS

First and foremost, I thank almighty Allah for his grace, protection, and for making this research a successful one.

Special gratitude goes to my supervisor Dr. Hany El Naggar, for his thorough guidance towards the success of this research. He is a kind-hearted individual whose commitment is targeted at student growth and achieving the best of results.

My sincere thanks also go to my senior colleagues Ahmed Mahgoub and Ahmed Moussa for their respective assistance during times of need in my findings.

I would also like to thank my parents for the contribution they have made in my life. Their words of wisdom and motivation during my program cannot be appreciated enough.

CHAPTER ONE

INTRODUCTION

Integral Abutment Bridges (IABs) have gained popularity due to their economic, functional, and durable features. The daily and seasonal variation in temperature subjects the span of integral bridges to increase and decrease; thereby, causing the abutment to press against the approach backfill and drag away from it. This cyclic displacement also leads to stress changes in the backfill soil, earth pressure on the abutments, and stress supporting piles. Consequently, the integral bridge components, approach backfill, and foundation soil experience cyclic loading and realizing their interconnection is crucial for successful design and acceptable performance (Arsoy et al., 1999).

However, the effects of the abutments' cyclic displacement on the soil-structure interaction are not fully understood, therefore the need for the 2-Dimensional finite element analysis. This research aims to validate the employed soil models by predicting the soil mass's earth pressure and the earth's pressure acting against the abutment. The finite element models will emulate the geometry, materials' settings, and cyclic displacements as the monitored structure in New Brunswick and the two results over the cycles compared. More importantly, a parametric study will further investigate the performance of different backfill alternatives due to extreme cyclic loadings. Each backfill material was analyzed at different drainage widths to investigate the effect on their performance. A total of seven backfill materials; TDA, Expanded polystyrene (EPS) Geofoam, Lightweight Expanded clay aggregate, EPS composite soil, Pit-run gravel, Gravel A1 and Crushed Stone, were investigated in this research.

1.1 Statement of The Problem

The major challenge integral bridges encounter is that the expansion and contraction of the whole structure against the backfill material causes a complex soil-structure interaction problem. Different design methods and the cyclic effect of the thermal load lead to the complex evaluation of the earth pressures and structural behaviour with time (Springman et al. 1996; Wood and Nash 2000; Cosgrove and Lehane 2003; Clayton et al. 2006). In reaction to this challenge, engineers and researchers have presented several propositions and design recommendations (Kunin and Alampalli 2000; Hassiotis et al. 2005), but an agreement on a genuine design approach is still not accomplished.

1.2 Background Overview

Like conventional bridges, IABs design comes as single or multiple span structures with a continuous concrete deck. The abutments of IABs rest on flexible foundations to accommodate the longitudinal forces through movements rather than expansion joints, as in typical bridges. According to GangaRao et al. (1996), designers may construct the supporting pier in multi-span bridges integrally or independently of the deck.

Typical bridges consist of expansion joints and bearings that aids in accommodating the expansion and contraction of the bridge due to the different daily and seasonal temperature changes. Bearings replacement requires lifting the bridge, possible limitation on the structure, or, in some cases, the total shutdown. Consequently, the construction of integral bridges as an alternative in many countries is rampant (Huntley, 2009). A typical pile-supported integral abutment design layout is shown in Figure 1.1

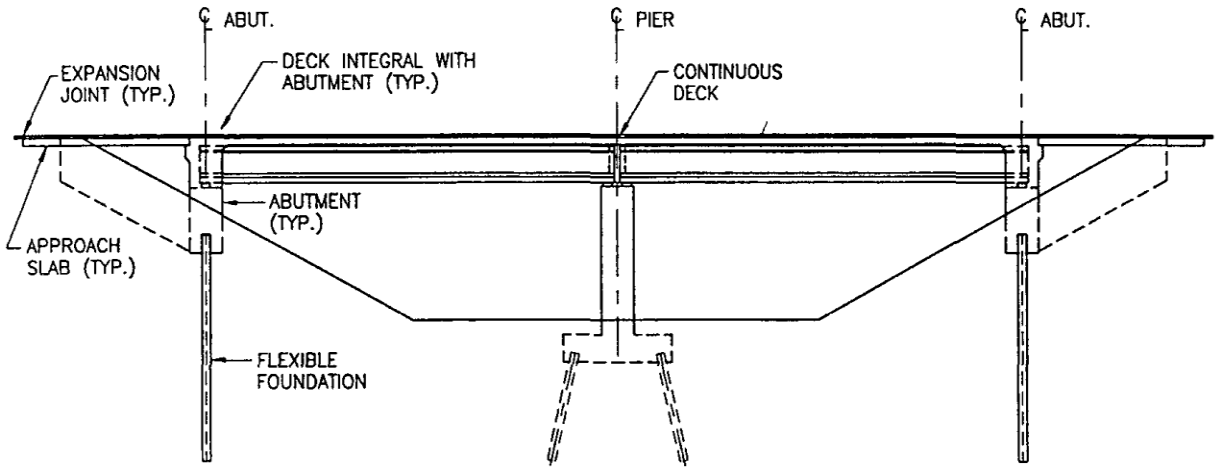

Figure 1.1: Typical integral abutment bridge design details (Husain and Bagnariol 1996).

Despite the increasing construction of IABs, there is still no worldwide accepted design approach. However, the Canadian Highway Bridge Design Code (CAN/CSA-S6-06) concisely evaluates integral abutment bridge design. As declared in the code, these bridges' structural analysis should meet pertinent demands familiar to slab and deck-on-girder bridges. The bridge engineer should also adopt elastic analysis when calculating the negative moment near the integral abutment. It should also include any in-plane forces and bending moments caused by structural assemblage once continuity between the superstructure and the substructure has been achieved. The American Association of State Highway and Transportation Officials (AASHTO) Load Resistance Factor Design (LRFD) Bridge Design Specifications (2007) briefly discusses integral abutments stating that the abutments should be designed to resist or absorb creep, shrinkage, and thermal deformations of the superstructure.

These unsolved challenges gave rise to the need for further research on Integral Abutment Bridges to conclude a universal and widely accepted design and analysis method by engineers (Huntley, 2009).

1.3 Thesis Contributions and Objectives

This thesis aims to discover the most suitable backfill materials for integral bridges through the understanding of soil-structure interactions, and the objectives are stated as follows:

1. Investigate a research project on the field performance and evaluation of an integral abutment bridge in Fredericton, New Brunswick.
2. Execute finite element analyses on the bridge east abutment's soil-structure interaction and the supporting pile foundation under cyclic loadings.
3. Evaluate the employed soil models' effect on the predicted earth pressure within the soil mass and the earth pressure acting against the abutment.
4. Use the validated constitutive model to analyze the performance of different backfill options for integral bridges.

1.4 Thesis Outline

Thesis Statement: Adoption of low-stiffness drainage backfills will help improve the long-term safety and reduce the design cost of integral bridge abutments.

I. Introduction

A. Statement of the problem

1. Complex soil-structure interaction of integral abutment bridges.
2. Lack of generally acceptable design approach amongst bridge engineers.

B. Background overview

1. Canadian Highway Bridge Design Code (CAN/CSA-S6-06) and American Association of State Highway and Transportation Officials (AASHTO) Load Resistance Factor Design (LRFD) bridge design specifications.

C. Thesis contribution and objectives

II. Literature review

A. Development and design practice of integral bridges

1. Evolution of integral bridges and the New Brunswick Department of Transportation and Infrastructure (NBDTI) standards and specifications.

B. Past research works on integral bridges

1. This section reviews the surveys, field projects and numerical analyses that were conducted on jointless bridges.

C. Field case study: The route 2 high-speed connector underpass

1. Intensive study and relevant field data were obtained from the monitored structure.

III. Research Methodology

A. Development and validation of a two-dimensional finite element model

1. The results of Mohr-Coulomb and Hardening soil models were compared to the monitored field results following the same geometry, construction procedure and cyclic loadings.

B. Investigation of the viability of various backfilling options

1. The validated hardening soil model and a linear-elastic model determine the performance of different backfill alternatives by estimating their

respective magnitude of lateral earth pressure under extreme cyclic loadings.

2. Long-term analyses were conducted on the most efficient drainage backfills.

IV. Results and discussions

A. Isolation efficiency

B. Lateral earth pressure coefficient ratio

C. Ground-level settlement

D. Long-term performance of the most efficient drainage materials

V. Conclusions

A. Research summary and conclusions

1. Overall research summary, deductions and recommendations are stated in this section.

CHAPTER TWO

LITERATURE REVIEW

2.1 Introduction

This chapter aims to give concise information on the development, essence, and most importantly, review relevant previous researches on integral bridges. This review shows that most research has targeted the improvement of jointless bridges with efforts to attain a more standardized design practice. Other necessary knowledge regarding the advantages and limitations of integral bridges over traditional types is also discussed in this chapter.

2.2 Development and Design Practice of Integral Bridges

The evolution of integral bridges began in the 1930s when the Ohio Department of transportation agency first showed interest in achieving continuity in bridge superstructures. For many decades, the agency adopted riveted, butt-welded, and high-strength bolted field splices to attain continuity in jointed bridges. Additional efforts were also made to control problems associated with the penetration of de-icing chemicals into expansion joints by using elastomeric compressible seals in the United States. However, most of these seals showed deterioration and failure over time, while others required consistent maintenance. Consequently, bridge engineers switched their attention to a reliable alternative – Integral bridges (Martin and Burke, 2009). There are four classes of Joint-less bridges: Abutmentless bridges, Slip joint bridges, Flexible arch bridges and Integral Bridges (Horvath 2000, Arsoy et al. 1999).

In 1995, The New Brunswick Department of Transportation and Infrastructure (NBDTI) began constructing integral abutment bridges. Located in Chatham's parish, the Harper Road Overpass was the first IAB built in New Brunswick. The bridge is a one-span reinforced concrete structure spanning 33 meters. Over 52 Integral and Semi-Integral bridges have been constructed in New Brunswick since 1995, with lengths varying between 24 and 133 meters. The 2015 Structural Design Standard released by NBDTI limits an integral bridge's skew angle to 20 degrees and maximum length to 100 meters. The NBDTI Standard detail for an IAB backfill is shown in Figure 2.1, with compression foam and geo-composite systems installed directly behind the concrete abutment. Geogrid materials are placed at various 600mm thicknesses behind the abutment, and the Borrow D material consisting of 75mm crushed rock is sandwiched between these geogrid layers. Finally, the approach slab is installed on top of a 31.5mm crushed gravel layer with two sheets of 6 mil polyethylene between the slab and the crushed gravel (NBDTI standards and specifications 2015).

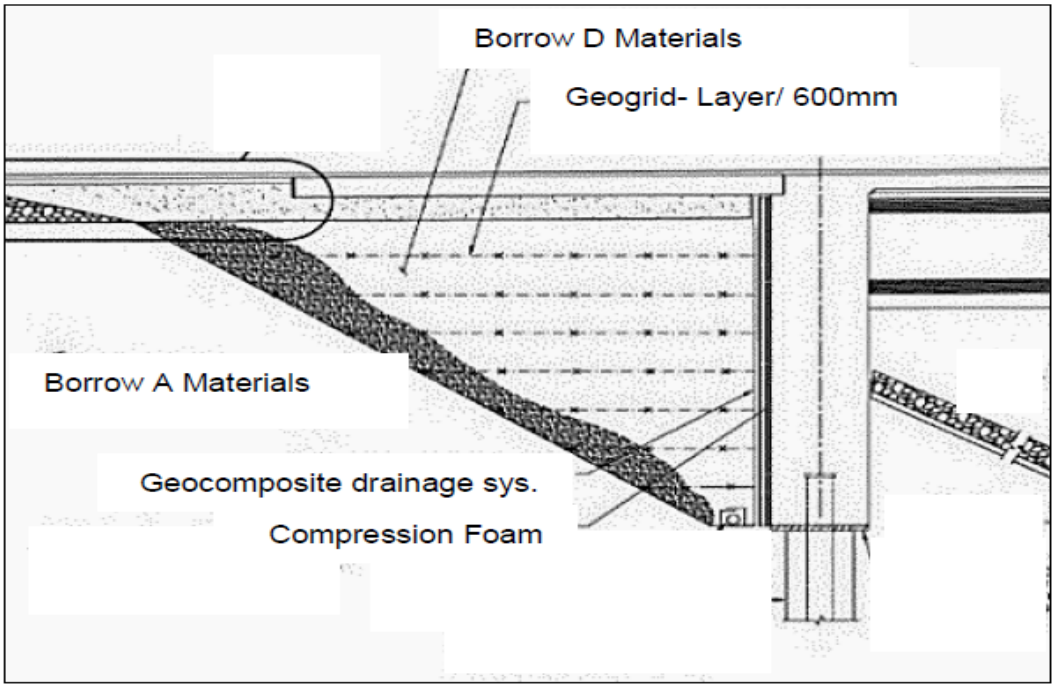

Figure 2.1: IAB Standard Backfill Detail (NBDTI standards and specifications, 2015).

Advantages and Limitations of Integral Bridges

The progression of integral bridges, which were primarily adopted to eradicate the problems emerging from joints leakage, got interesting as more advantages and fewer limitations of these bridges were discovered over conventional ones.

2.2.1 Advantages of Integral Bridges

According to Martin and Burke (2009), the advantages of an integral bridge are not only reduced to the bridge's initial cost and life-cycle cost, but they also reduced the price of its future renovation (e.g., expansion) and its ultimate substitution.

More advantages of integral bridges over typical bridges are as follows:

- Compared to conventional bridges, construction costs and maintenance costs are much lower (Arsoy 2000, Arockiasamy & Sivakumar 2005; Lawver et al. 2000, Hong et al. 2003).
- The construction of integral bridges is rapid and straightforward (Martin and Burke, 2009).
- Integral abutments provide high redundancy, boost load distribution at the supports and provide more effective overall structural systems, specifically under seismic loading (Jayaraman & Merz 2001, Faraji et al. 2001, Martin and Burke 2009).
- Lesser piles without battering are sufficient for foundation support than typical bridges (Arsoy 2000, Mistry 2005).
- The vehicle riding quality on an integral bridge is more comfortable and smooth since there are no expansion joints (Mistry 2005, Martin and Burke 2009).

2.2.2 Limitations of Integral Bridges

The following are some limitations to be considered while designing integral bridges.

- Constant temperature-influenced cyclic movements of abutments and traffic load result in settlement of approach fill and wedge near abutments (Hoppe & Gomez 1996, Arsoy et al. 1999, Xu 2006, Ooi et al. 2010a).
- They are not preferred when subsoil or embankments are of insufficient strength (Comisu and Gheorghita, 2010).
- Cyclic changes in earth pressures on the abutment tend to influence the rotation of integral bridges with skewed or curved geometry (Hoppe & Gomez, 1996; Arsoy et al., 1999).
- The reduction of axial load capacity and increased plastic hinges of piles due to high cyclic displacements is possible in integral bridges (Duncan & Arsoy 2003, Comisu & Gheorghita 2010, Ooi et al. 2010a). The foundation should be designed considering this point.

The rotation and contraction of the superstructure, differential settlement, creep, shrinkage, thermal stress, and earth pressure can lead to cracks in the bridge's wing walls and other concrete members (Ooi et al., 2010a).

2.3 Types of Abutments in Integral Bridges

According to the North American Study Tour Report, eight recommendable types of abutments are compatible with different locations of integral bridges (Cooke, 2003).

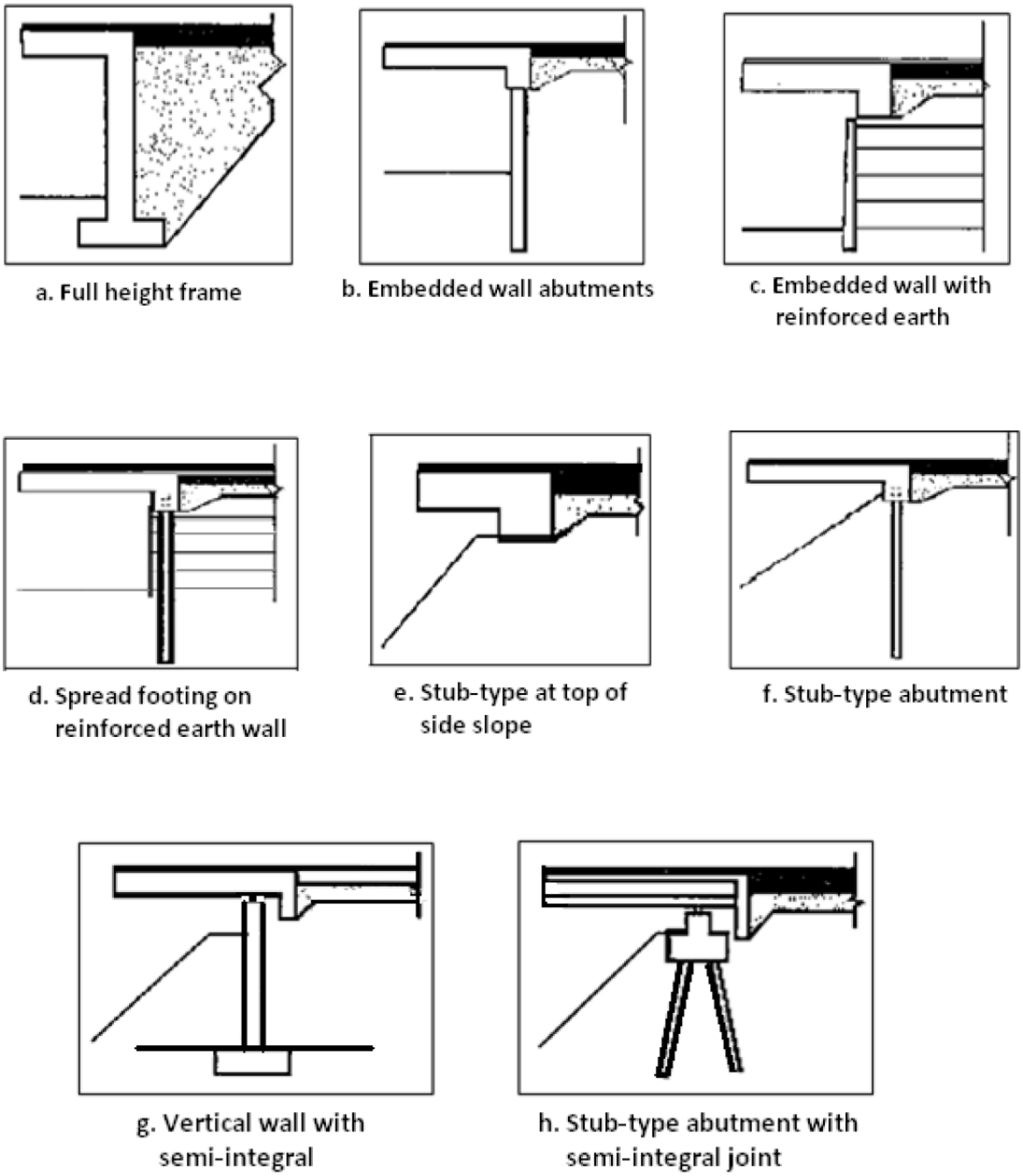

Figure 2.2: Types of abutment recommended by The North American Study Tour Report (Cooke, 2003).

The most encouraged and endorsed abutment is the stub-type abutment. Its simplicity and good performance with time have made it the most approved abutment type amongst bridge engineers.

2.4 Past Research Works on Integral Bridges

Field monitoring, numerical modelling and surveys were conducted over the years to broaden the understanding of how integral abutment bridges and the backfill materials behave and interact.

2.4.1 Integral Abutment Bridge Surveys and Practices

Over the years, researchers have conducted surveys on several design practices to evaluate integral bridges and how they can be improved in the future. The integral abutment bridges studied in New York, U.S and Ontario, Canada gave good remarks regarding performance and overall service like the typical bridges in the regions (Alampalli & Yannotti 1998; Husain & Bagnariol 2000). However, further recommendations on the development of IABs were made by other authors. Soltani and Kukreti (1992) suggested that the U.S. highway departments' design practices construct longer integral abutment bridges in the United States to scrap the conservative approach used in the past. (Hambly 1997; Van Lund & Brecto 1999) at the end of their study conducted across the U.K, U.S and Sweden, also encouraged the demand to construct more jointless bridges with approach slabs as maintenance issues will be limited. According to the survey done by Knickerbocker et al. (2003) in Tennessee, the U.S, high-performance concrete with higher strength and durability should be incorporated with integral abutments design for all-time satisfaction. Husain et al. (2005) then investigated the Moosecreek bridge in Canada, i.e. a model bridge and the elongation of its prefabrication system to multi-span bridges was proposed for full performance. Maruri and Petro (2005) later reviewed a 2004 survey summary on Integral Abutments and jointless bridges in Columbia and Puerto Rico, and the granting of a federal utility scheme on Integral bridges was also suggested.

2.4.2 Field Instrumentation and Monitoring

Aside from surveys, field projects regarding integral bridges were also instrumented and assessed to highlight potential setbacks with necessary corrective measures to ensure they are within scope. These instrumentation works led to more valuable conclusions and recommendations from various researchers. Girton et al. (1991) first suggest that piles supporting the abutment of integral bridges should be oriented along their weak axis and battered along their lateral direction to improve flexibility and reduce horizontal motion, respectively. According to Darley and Alderman (1995), in their research conducted in Northamptonshire, United Kingdom, the deck of rigid frame integral bridges should not be cambered as it will not aid the accommodation of thermal expansion. (Darley et al. 1998; Barker and Carder 2001) also proved that the monitored lateral earth pressure behind integral bridges' abutment would increase density under cyclic loading, and its future investigation should be considered. To improve the behaviour of concrete integral bridges, engineers should also consider reducing the length of prestressed girders and the impacts of creep and shrinkage on these structures (Barker and Carder 2001; Huang et al.2005; Fennema et al. 2005). In addition to these contributions, a vital recommendation regarding abutment-pile connection was presented by Frosch et al. (2005). Their research in the United States suggested that the connection between abutments and piles should be pinned to eradicate the piles' double curvature reaction to cyclic loading.

2.4.3 Numerical Analyses

Numerical modelling is a widely accepted method of solving tedious engineering problems by computational simulation of field cases. The instrumentation cost and time needed to complete

field research projects made researchers find this alternative approach towards achieving the same accurate results (Huang et al., 2005; Kim and Laman 2012). Thippeswamy and GangaRao (1995) first conducted analyses on five in-service jointless bridges subjected to various forms of loads as they showed the results from only one of the bridges. The researchers concluded that integral bridges resting on flexible pile foundations experience less stress from loading cases at the superstructure/abutment joints than those supported by spread footings. They also stated that top small compressive stress and bottom large tensile stress were discovered at the flexible foundation structures' superstructural midspan. The form in which earth pressure is gathered behind an integral abutment and the abutment's bending moments were later investigated by Wood and Nash (2000) using the FLAC finite difference program. This numerical analysis showed that the mid-height horizontal earth pressure and the negative moment around the abutment largely depend on the backfill and abutment stiffness. This result means that an increase in the backfill stiffness will lead to a corresponding increase in stresses near the top of the backfill and the abutment moment.

Despite these intensive and remarkable researches over the years, none has established proven criteria for selecting a backfill material for integral bridges. According to Arockiasamy et al. 2004 and Ooi et al. 2010a, the magnitude and distribution of backfill soil pressure are still not fully acknowledged. Therefore, it is essential to understand integral bridges' behaviour and how these backfill pressures influence them.

CHAPTER THREE

CASE STUDY: THE ROUTE 2 HIGH-SPEED CONNECTOR UNDERPASS

3.1 Project Description

The Route no. 2 High-Speed Connector Underpass was constructed by NBDOT in October 2004 and was monitored by Huntley (2009) as partial fulfillment of her Ph.D. degree. The field data used in developing the 2D finite element models (FE-models) are obtained from this two-38-metres-span Integral Abutment Bridge.

Huntley (2009) reported that the monitored bridge has a total width of 17600mm, with the superstructure consisting of eight prestressed concrete girders spaced at 2200mm. Each New England Bulb Tee girder (NEBT 1800) height of 1800mm, supporting a 225mm thick reinforced concrete slab. Expansion joints are omitted as these girders are rigidly connected to the east and west abutments. The bridge deck also consists of concrete barrier walls on both sides of its longitudinal span, with a 1940mm wide sidewalk located along its north side alone, leading to an unsymmetrical geometry.

The concrete girders rest on elastomeric bearing pads at the centre pier, and the approach slabs are firmly connected to the abutment walls. Also, the structure accommodates three lanes of vehicles, two moves in opposite directions, and the middle lane cuts to permit turning onto the highway lanes (Figure 3.2).

Figure 3.1: Route No. 2 High-Speed Connector Underpass selected for instrumentation (Huntley, 2009).

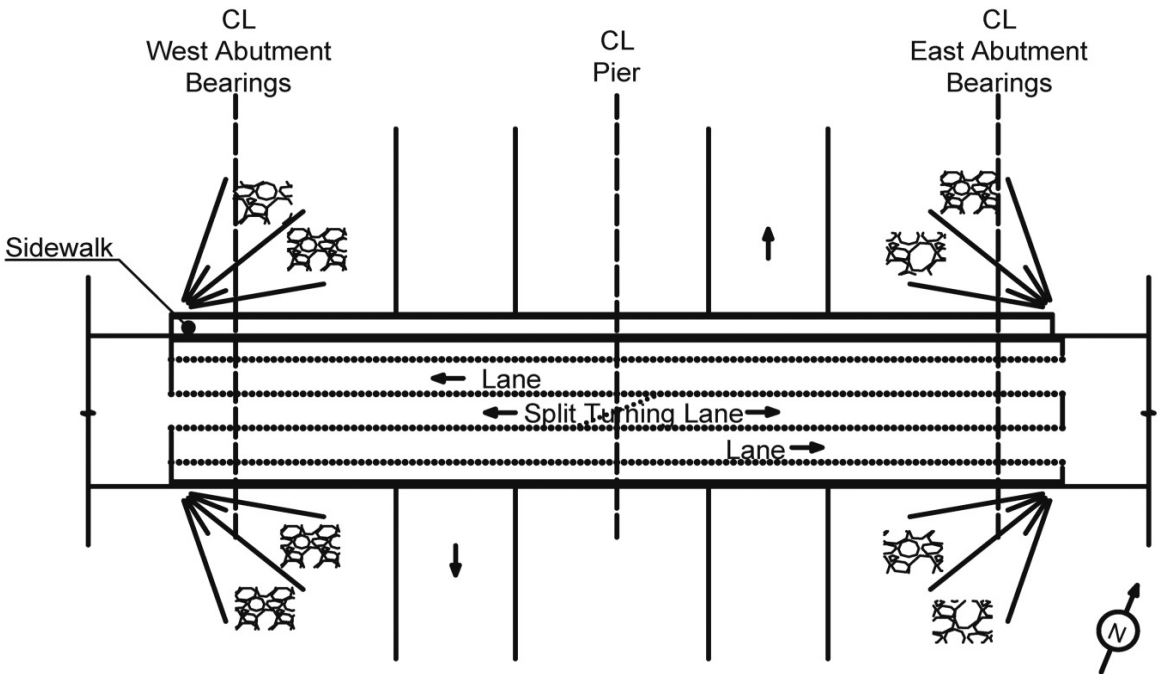

Figure 3.2: Plan view of Route 2 high-speed connector underpass (Huntley and Valsangkar 2013).

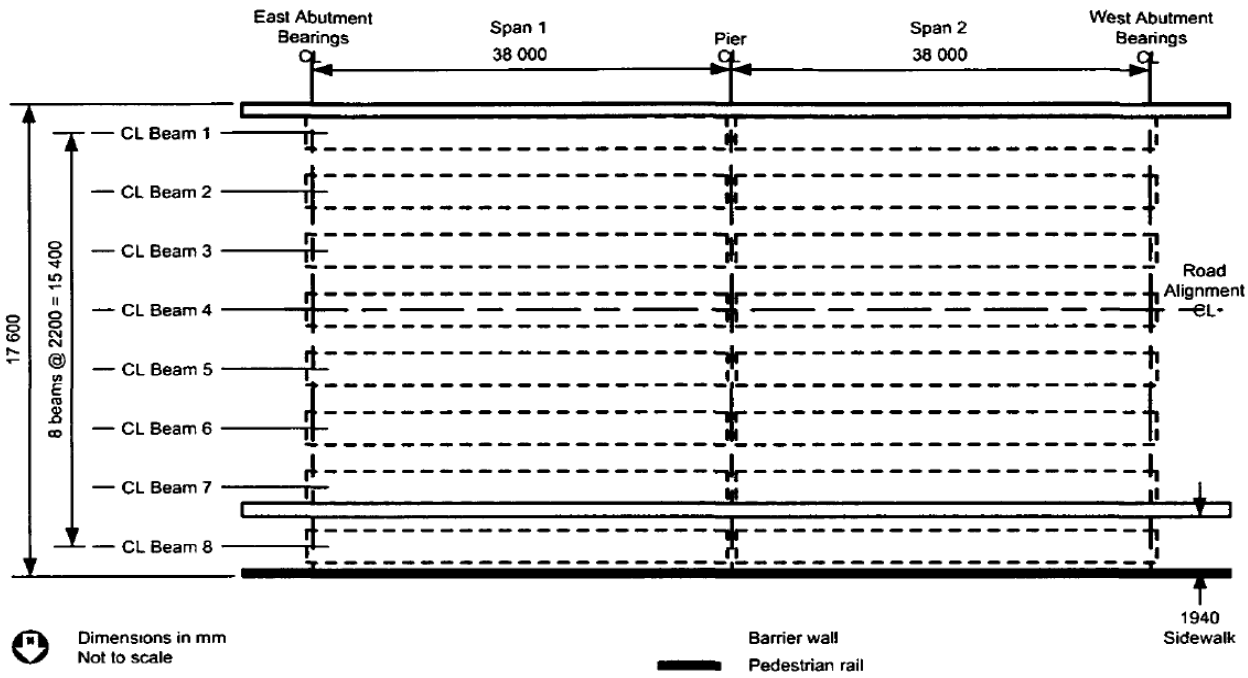

Figure 3.3: Superstructure detail of the integral abutment bridge selected for monitoring (Huntley, 2009).

Many piles were used to support the structure; the abutments were built on 15 HP310xl32 steel piles, while 22 HP310xl32 steel piles support the centre pier. Most of the pier piles are battered at a slope of 4V:1H in traffic direction, and they are oriented for strong axis buckling. In contrast, the rest of the pier piles are oriented for weak axis buckling with the same slope battering but in the lateral direction. Weak axis orientation is adopted for the abutment piles and backfilled with loosely placed granular material for smooth displacement. The piles' top 3000mm are installed in this 1200mm wide trench of loose granular material. The east and west abutments are 4405mm and 4593mm, respectively, and both are 1200mm thick.

A 1500mm thick drainage layer is used behind each abutment, and they are backfilled with Borrow A materials. The adopted Borrow A material is free from Mudstone, claystone, siltstone, clayey or silty soil and has maximum dust content of 25%. Its material properties were also defined

through a direct shear box and sieve analysis. Field compaction of the Borrow-A materials took place at every 200mm lifts to a minimum of 95% of the maximum dry density, which averaged 2200 and 2170 kg/m^3. The backfilling layers do not entail geofoam, geocomposite drainage system, or reinforced earth for strengthening (Figure 3.4).

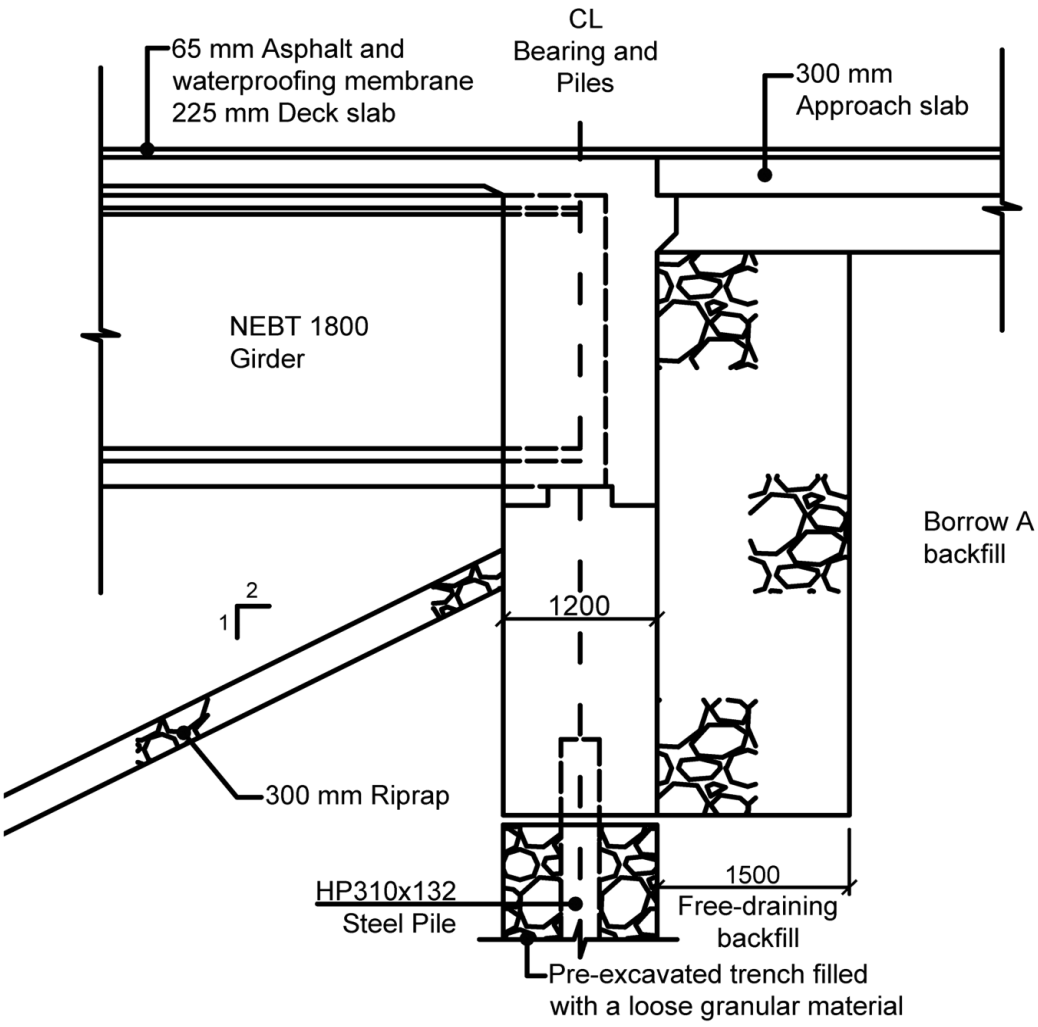

Figure 3.4: Profile and dimensions of the east abutment and backfilling materials in millimetres (Huntley and Valsangkar 2013).

3.2 Construction Timeline

The Route 2 Underpass construction began on July 21, 2003, and continued till its completion on September 3, 2004. Table 3.1 below gives a breakdown of the construction progress.

Table 3.1: Route No. 2 High-Speed Connector Underpass Construction Timeline (Huntley, 2009).

Event description	Date
Work commenced	July 21 2003
H-piles arrived on site for the pier footing	July 21 2003
Driving of H-piles commenced	July 21 2003
Pier footing concrete placed	Sept 5 2003
West abutment footing concrete placed	Sept 19 2003
East abutment footing concrete placed	Oct 28 2003
Bridge girders arrived on site and placement began	Nov 28 2003
Placement of bridge girders completed	Dec 4 2003
Deck pour with west abutment portion	May 28 2004
Deck pour with east abutment portion	June 16 2004
Commenced backfilling of west abutment	June 28 2004
Commenced backfilling of east abutment	June 29 2004
Approach slabs poured	July 14 2004
Finished paving the structure and approaches	Sept 3 2004
Opened service road and structure	Oct 19 2004

3.3 Instrumentation

Table 3.2 states all the instruments used for the structure, as Vibrating wire (V.W.) sensors are the most used field research instruments. Incorporated in each V.W. sensor is a thermistor that

gives temperature data in inclusion to sensor reading. Factory calibration was conducted on the V.W. sensors, and more calibration tests were done at the University of New Brunswick.

Table 3.2: Route No.2 High-Speed Connector Underpass instrumentation summary (Huntley, 2009).

Instrument	Quantity	Location	Installation date
VW strain gauges	30	Abutment piles	July – August 2003
VW concrete embedment strain gauges	40	Bridge girders and deck	Nov 03, May – June 04
Thermocouples	24	Bridge girders and deck	Nov 03, May – June 04
VW contact earth pressure cells	6	Abutment walls	June 2004
VW tilt meters	4	Abutment walls	June 2004
VW deformation meters	4	Abutment walls	June – July 2004
Fiber optic sensors	7 pairs	Abutment backfill	June 2004

The instrumentation was done for roughly one year, and every device cable was routed from separate instrument points to a central spot on both abutments via a safe conduit. There are three multiplexers positioned at these central points on the abutments with a datalogger at one of the sites. This datalogger accumulates and keeps multiplexer sensor data at 20 minutes intervals, and data is occasionally downloaded for analysis.

3.3.1 Tilt Meters

The rotational movement of each abutment was measured using tilt meters. These tilt meters were oriented in the traffic direction to calculate the temperature-dependent rotation of the abutments. Tilt meters were located on either side of the bridge seat and at opposite ends of the

abutment centre line and were also positioned to measure rotations at the top, bottom, right, and left end of the bridge.

Each abutment consists of Two Geokon models, 6350 vibrating wire Tilt meters installed at their respective inner faces before backfilling. The Tilt meters were placed horizontally at around $^1/_3$ and $^2/_3$ of the abutment length and spaced vertically at about $^1/_3$ and $^2/_3$ of the abutment height (Figure 3.5). Protective boxes were made at the installation points, and the tilt meters were bolted within these enclosures aligned with the abutment inner surface.

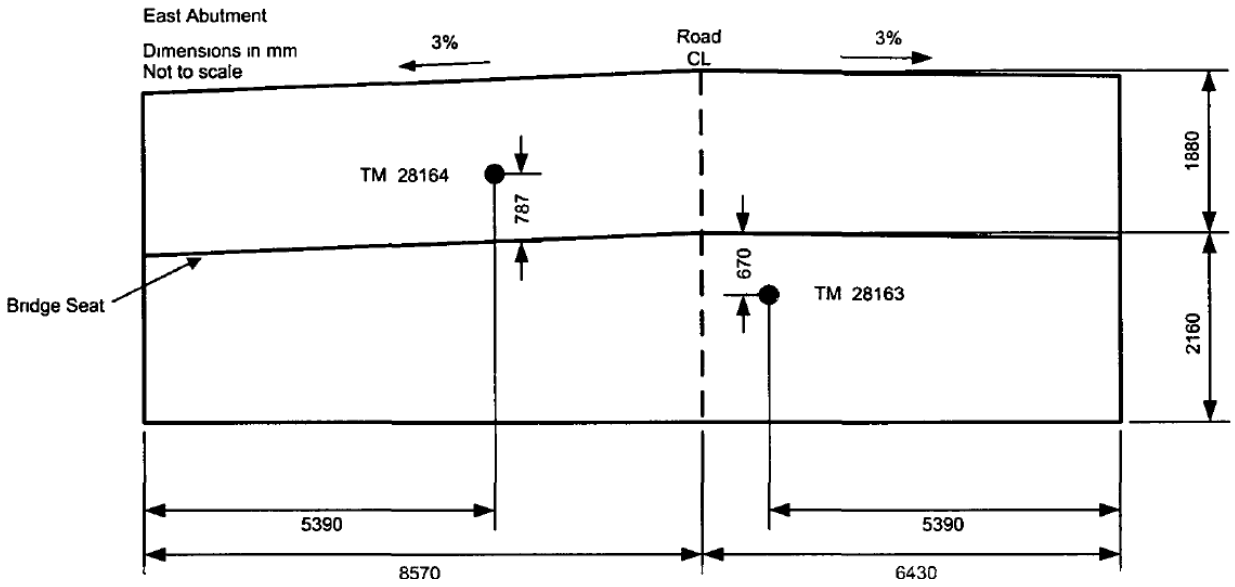

Figure 3.5: Tilt meter locations on the east abutment. A similar configuration was used for the west abutment (Huntley, 2009).

3.3.2 Deformation Meters

In contrast to tilt meters, Deformation meters were used to measure the abutments' translation in the traffic direction. Similarly, the deformation meters were placed on either side of

the bridge seat and on opposing ends of the abutment centerline. This arrangement resulted in estimating the lateral translation at the top, bottom, right, and left-hand sides of each abutment.

Each abutment was equipped with two Geokon 4430 vibrating wire deformation meters. Opposite the tilt meters, the sensors were positioned horizontally at around $^1/_3$ and $^2/_3$ of the abutment length and were spaced vertically at about $^1/_3$ and $^2/_3$ of the abutment length (Figure 3.6). The installation of the deformation meters at the inner face of the abutments was done during the backfilling procedure. Although, the backfill had to be at the installation point level before each sensor was installed. Shallow trenches of the same length as the deformation meters were dug once the backfill reaches the required level. The deformation meters were bolted to the abutments' inner faces and positioned in the trenches.

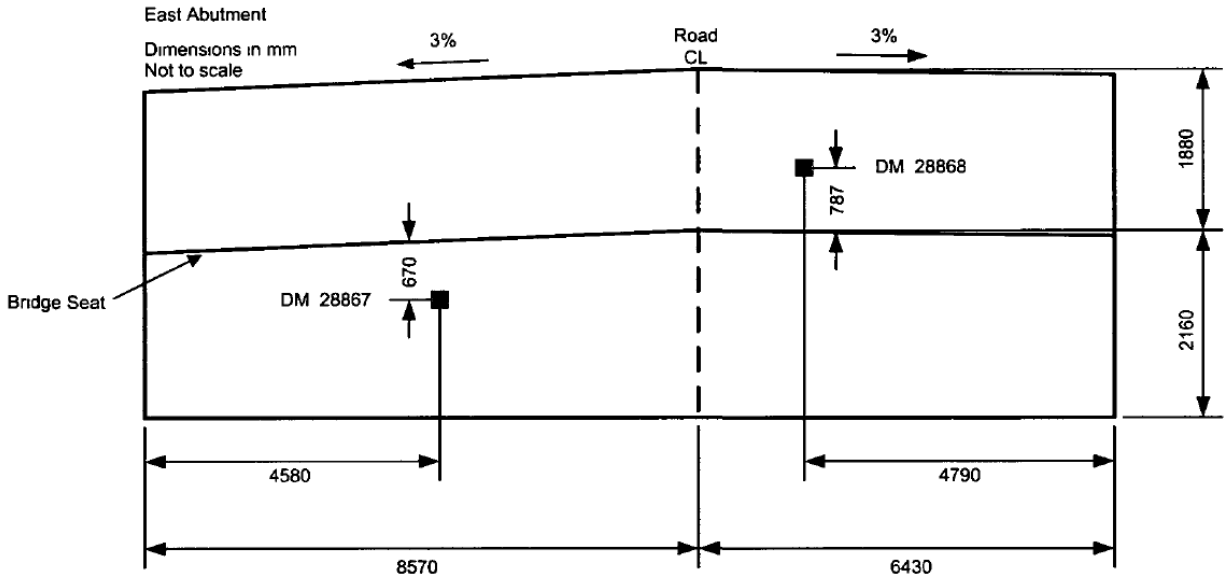

Figure 3.6: Deformation meter locations on the east abutment. A similar configuration was used for the west abutment (Huntley, 2009).

3.3.3 Contact Earth Pressure Cells

Three Geokon models 4810 vibrating wire contact pressure cells were installed on each of the abutments' inner faces to estimate the earth pressures acting on them. These pressure cells are situated along the centerline of the abutment at elevations of around $^1/_4$, $^1/_2$ and $^3/_4$ of the abutment height (Figure 3.7). At the start, enclosures for the pressure cells were established on the formwork before abutment concrete pour. A smooth surface between the concrete wall and the sensors was achieved upon removing the formwork and installing the pressure cells in these enclosures. Each instrument was first shielded with sand to protect the pressure cells from direct touch with larger rocks in the backfill.

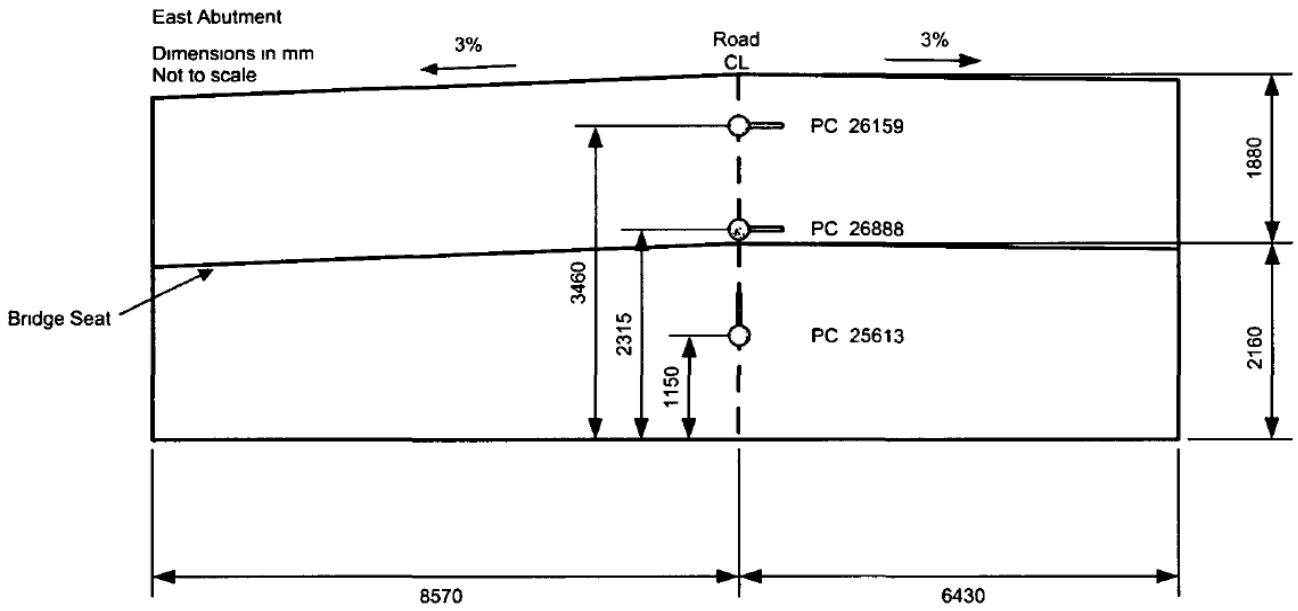

Figure 3.7: Pressure cell locations on the east abutment. A similar configuration was used for the west abutment (Huntley, 2009).

Figure 3.8: Locations of contact pressure cells installed on the west abutment. Installation locations were similar for the three contact pressure cells mounted on the east abutment (Huntley and Valsangkar 2013).

3.3.4 Strain Gauges

The pile strains were quantified using strain gauges installed on the abutment piles at the top 1.65m of the loose granular material zone. This upper region is termed to be the most critical as far as lateral load response is concerned. Different elevations within this area were instrumented to estimate the strain's distribution and the amount of yield. The strain results were then used to compute axial loads, weak axis moments, and strong axis moments.

Thirty Geokon model VSM-4000 vibrating wire strain gauges were installed on the abutment foundation piles at the end of piling works. An internal pile and an external pile on each

abutment were selected for mounting the strain gauges. Figure 3.9 gives a plan view of the abutment piles with the chosen piles circled and numbered for instrumentation. On the interior piles, gauges were mounted on three levels, and the exterior piles on two levels with three strain gauges mounted at each level. Figure 3.10 shows the location of the strain gauges on an inner and outer abutment pile. As shown in Figure 3.11, each strain gauge was mounted on the piles' flange. Fitting brackets welded to the flanges were used to place the gauges at each location, and over-head shields protected all instruments. The free-draining granular filling was finally poured into the trench to ensure the piles displace unimpeded.

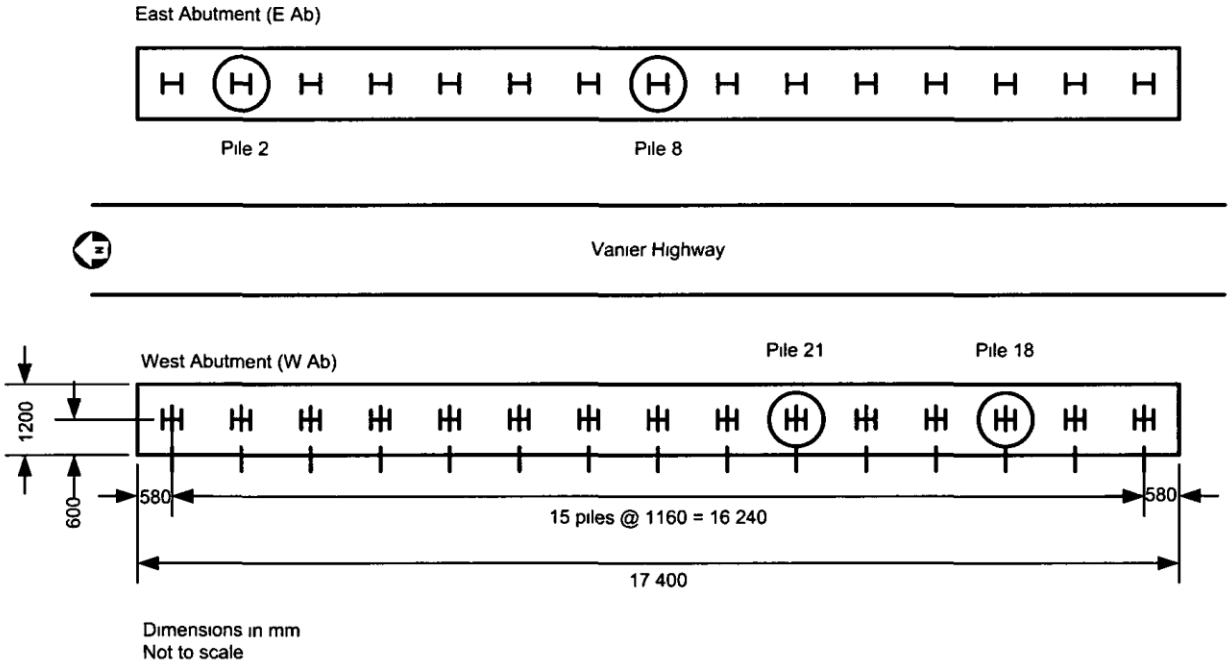

Figure 3.9: Plan view of abutment piles with the piles selected for instrumentation indicated (Huntley, 2009).

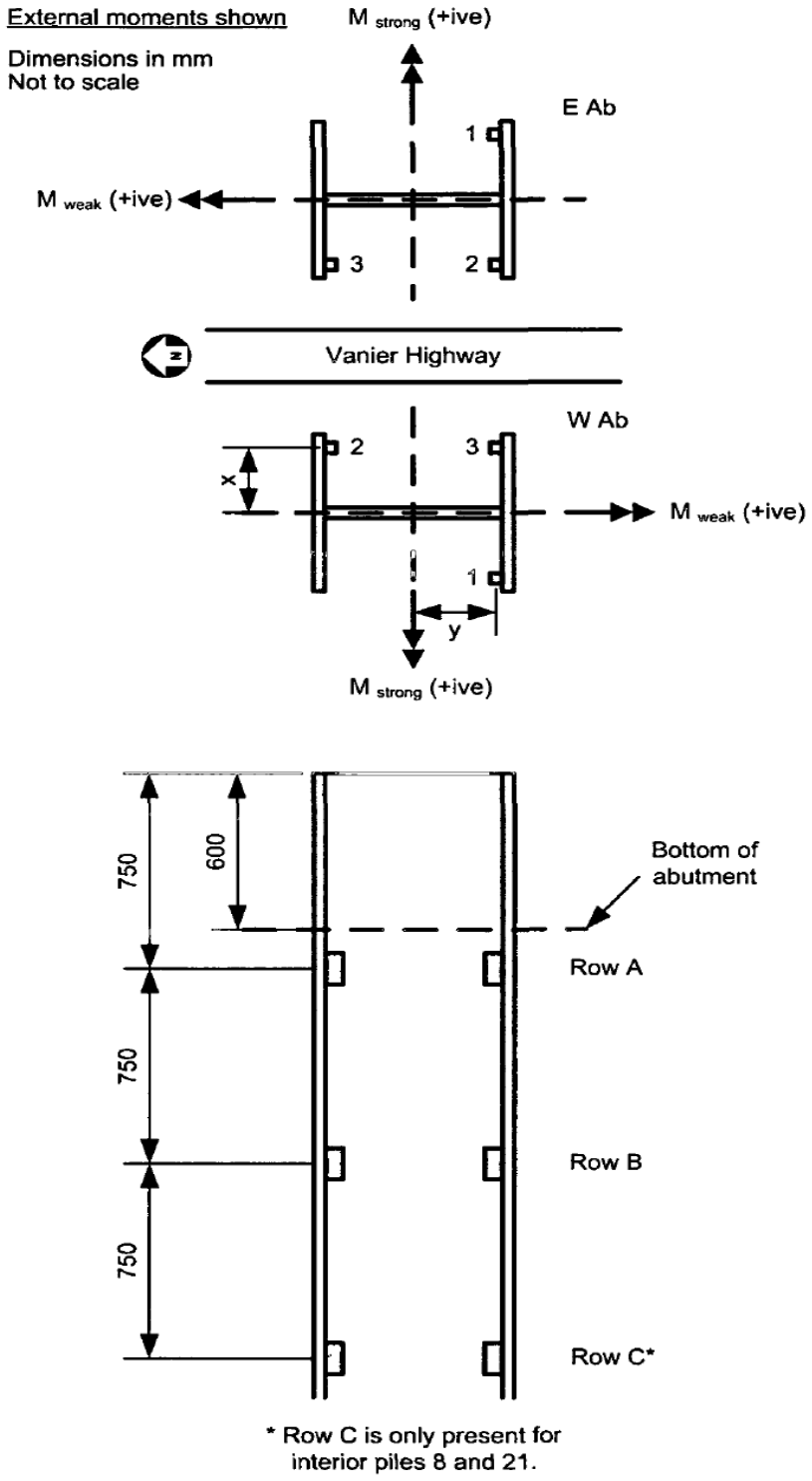

Figure 3.10: Location of strain gauges on the interior and exterior abutment piles (Huntley, 2009).

Figure 3.11: Strain gauge mounted on an abutment pile flange (Huntley and Valsangkar, 2013).

3.3.5 Concrete Embedment Strain Gauges

The girders and deck longitudinal strain and moments at the composite girder-deck region were estimated using Concrete-embedded strain gauges. Several elevations through the height of each girder were chosen for installation to ensure accurate strain distribution. At the end and

midspan of each interior and exterior girder, installation points were selected to estimate the strains and moments.

In total, 40 Geokon model VCE-4200 vibrating wire concrete-embedding strain gauges were installed. Thirty gauges were installed in four girders at ten spots (Figure 3.12). At each spot, strain gauges were installed at three different elevations, as shown in Figure 3.13. An extra gauge was installed in the bridge deck over each of the ten locations.

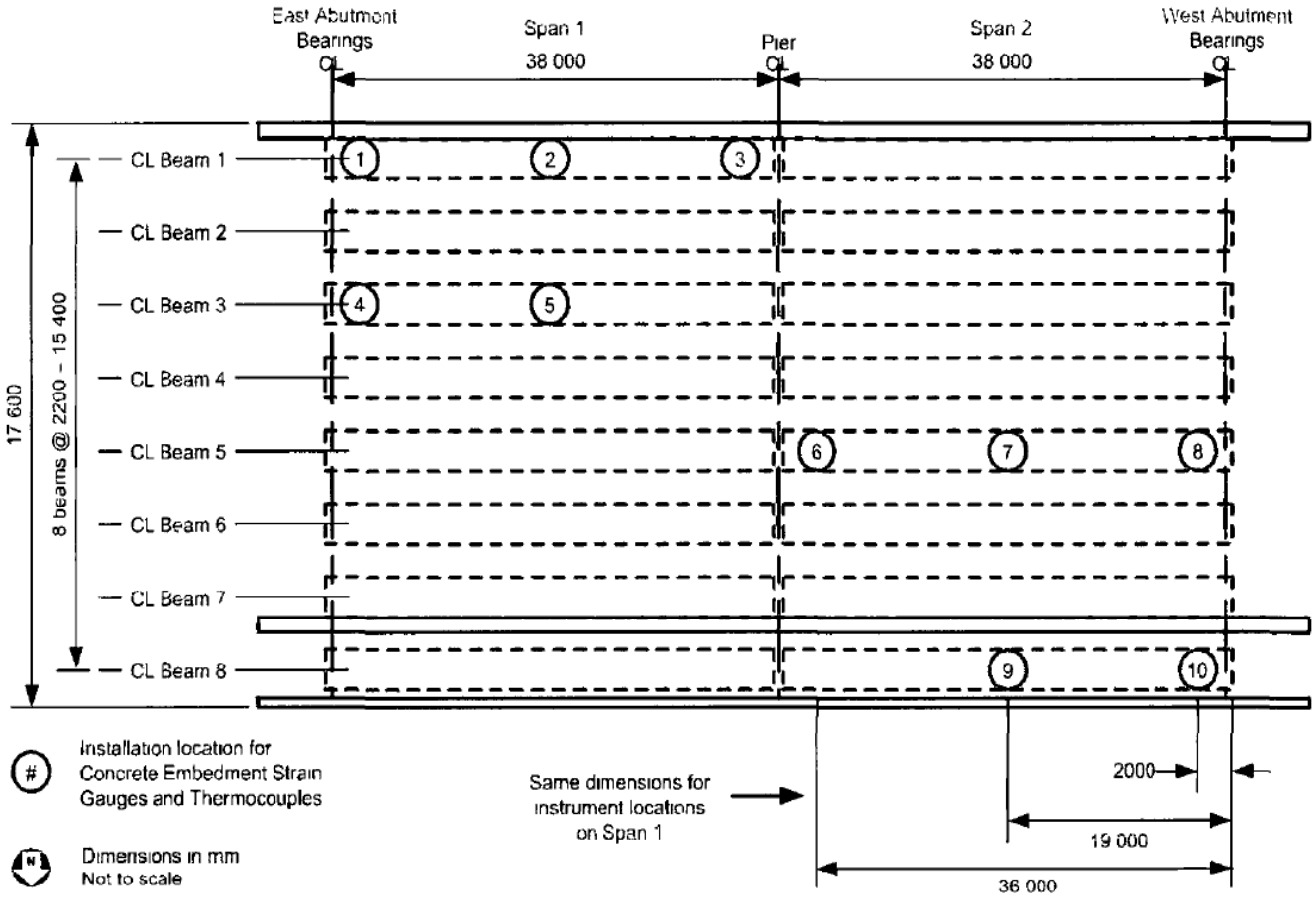

Figure 3.12: Instrumentation locations for the concrete strain gauges. The thermocouples are installed at locations 2, 5, 7, 9 only (Huntley, 2009).

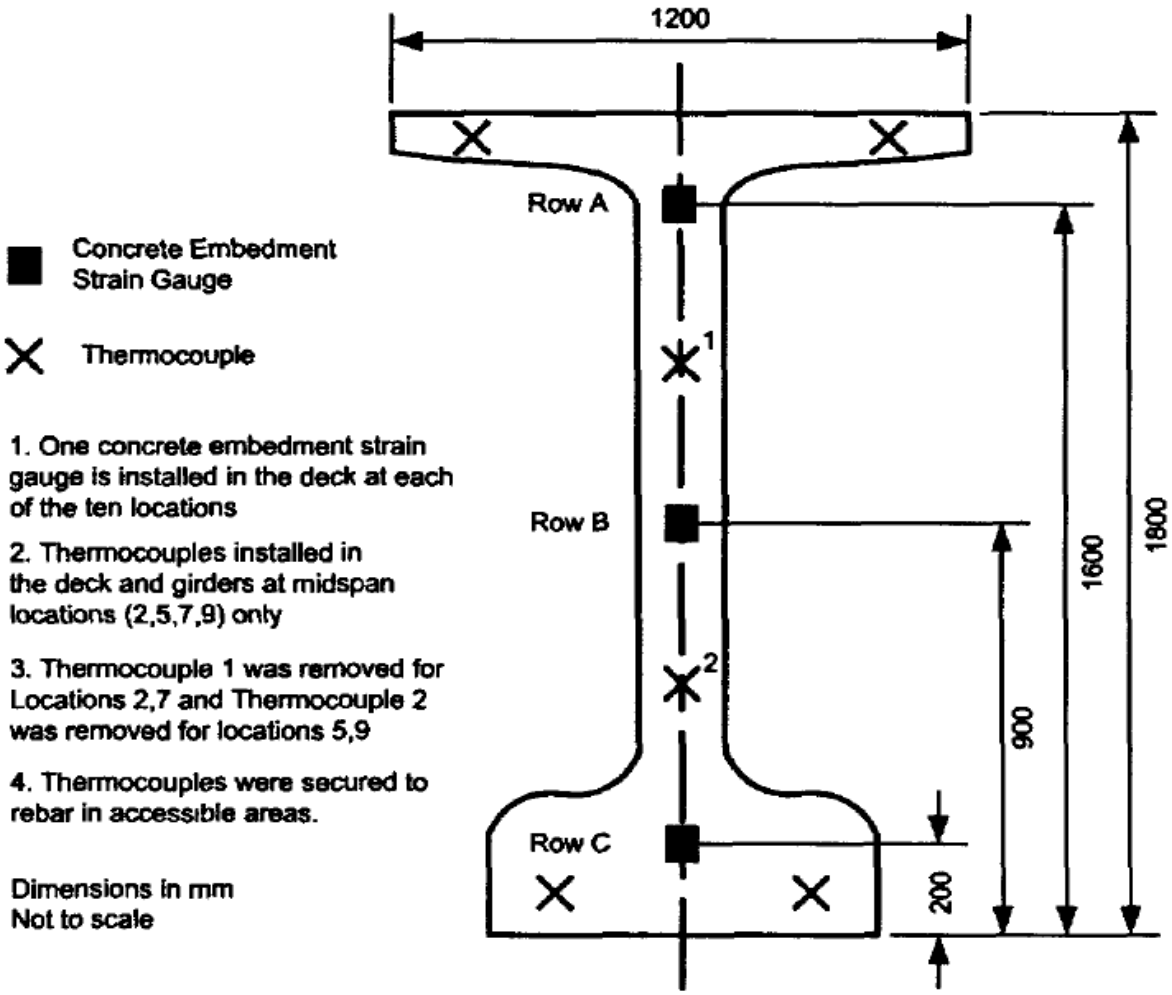

Figure 3.13: The cross-section view of the girder shows the concrete strain gauge and thermocouple installation locations (Huntley, 2009).

3.3.6 Thermocouples

The bridge girders and deck were equipped with twenty-four copper-constantan thermocouples. Additional temperature data for the bridge superstructure and the thermistor's figures with each vibrating wire sensor were delivered using thermocouples. Four of the ten girder spots chosen for the concrete embedding strain gauges (Figure 3.12) had five thermocouples

installed at divergent elevations, as shown in the girder cross-section (Figure 3.13). Also, each of the embedding gauge spots has one thermocouple installed in the deck.

3.3.7 Fibre Optic Sensors

Further details on the horizontal and vertical strain in the backfill behind the east abutment were obtained using Fibre optic sensors. These devices provide necessary measurement throughout their entire length.

In the backfill behind the east abutment, Seven pairs of fibre optic sensors were positioned. At 0.5 m, 2 m, and 6 m from the abutment's back end, the sensors were installed at identical depth as the deformation meters (Figure 3.14). The initial goal was to extend the fibres over the wing walls, but installing them on the field faced problems. When the backfill for the deformation meters reached installation grade, shallow trenches parallel to the abutment wall were dug and sand-lined before inserting the fibre optic sensors. Each trench was carefully covered with backfill and nominally compacted, similar to the deformation meters.

The fibre-optic sensors were split to 24 fibre-optic cables routed to the data acquisition system on the abutment wall's front to ease accessibility. Three different readings on the functioning sensors were taken on the site by a Brillouin optical time-domain analysis (BOTDA) system.

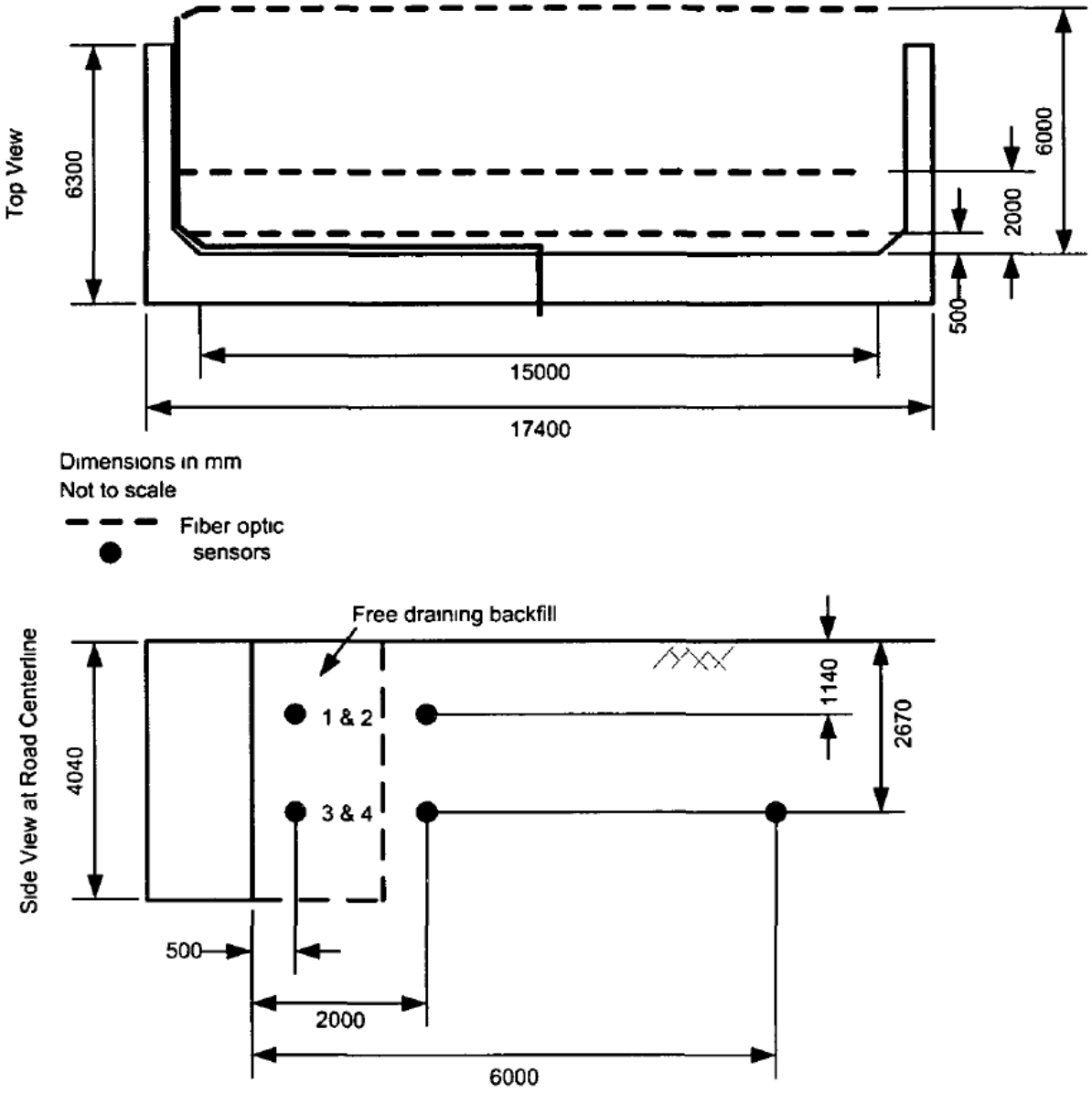

Figure 3.14: Fibre optic sensor locations behind the east abutment (Huntley, 2009).

3.3.8 Data Collection and Processing

Every 20 minutes, the data logger gathers and saves sensor data from multiplexers, and the data will be downloaded every month for review. Data are subsequently duplicated from each sensor and entered into a clear-cut spreadsheet. Dissimilar spreadsheets were made as each sensor

is distinctive to its gauge features and thermal calibration features. Every sensor's plots are updated, and the wrong data points are removed manually. Each sensor data is then averaged for each week at one data value. Eventually, summary plots for each sensor are updated with weekly averages. Weather data from Environment Canada are also necessary for continuous updating and compilation. The procedure of updating the spreadsheets and plots for a month of instrument and weather data takes a notable amount of time and is in the sequence of a couple of weeks.

3.3.9 Thermal Calibration of Earth and Contact Pressure Cells

In most cases, earth pressure and contact pressure cells are used to evaluate design predictions and get feedback to improve future designs. The use of pressure cells to determine the total amount of stress in soil requires that the cells are not too perceptive of non-uniform bedding. Also, the size of the cell should be such that non-uniformities at the local level are averaged. Eventually, both the installation and pressure cell properties do not remarkably influence a soil's stress level (Dunnicliff and Green, 1988).

3.3.10 Laboratory Temperature Calibration

Initial calibration was conducted on six vibrating wire hydraulic pressure cells installed in the field. Calibration tests were then carried out on a contact pressure cell similar to those installed in the field, as well as a new earth pressure cell. Table 3.3 describes the cells calibrated. Two tests were conducted based on Thompson (2005): an unloaded test and a loaded test. As a result of the unloaded test, the pressure cells were subjected to numerous temperatures, but they did not

undergo any external pressure. During the loaded test series, the pressure cells were exposed to several temperatures and externally applied uniform pressures. When tested under loaded conditions, pressure cells were exposed to several temperatures, and uniform pressures were externally applied. Unloaded tests were conducted first to rule out the possibility of thermal effects influencing the pressure readings. The load tests were then conducted to determine whether the effects of externally applied pressure and temperature could affect the output of the pressure cells.

Table 3.3: Details of the thermally calibrated 230 mm diameter hydraulic pressure cells.

Serial number	t/d ratio [1]	Full-scale pressure range (kPa)	Test conducted	
			Unloaded	Loaded
Field contact pressure cells [2]				
26158	0.052	350	x	
26159	0.052	350	x	
26886	0.052	700	x	
26888	0.052	700	x	
25612	0.052	1000	x	
25613	0.052	1000	x	
Contact pressure cell				
04-7935	0.052	350	x	x
Earth pressure cell [3]				
05-8284	0.026	700	x	x

[1]Dunnicliff and Green (1988) recommend that the t/d ratio be less than 1/10.
[2]Due to construction time restraints, the field cells were only thermally calibrated in an unloaded state.
[3]The earth pressure cell was tested at the University of New Brunswick as an undergraduate senior report (Thompson, 2005). However, the test results have been reanalysed for this research project.

3.3.11 Calibration Tests of Unloaded Cells

Several pressure cells were tested simultaneously in the unloaded condition in the environmental room, each cell being placed on a plywood sheet, as shown in Figure 3.15. After adjusting the room environment to the appropriate temperature, the room was given time to

acclimatize. Following temperature uniformity in the room and pressure cells, data was collected using hand-held readout units at well-ordered intervals for a period of three to four hours. The room temperature was then changed to the following degree and the process repeated. A total of six field cells were tested unloaded at room temperature and one negative temperature. Due to faulty cooling fans in the environmental room, the temperature could not be kept constant during these specific tests. In cells, #04-7935 and #05-8284, unloaded thermal tests were conducted after cooling fans were repaired. In these tests, temperature differences of -20°C, -10°C, 0°C, 10°C, and 20°C were evaluated.

Figure 3.15: Contact pressure cells being tested in an unloaded state (Huntley and Valsangkar, 2013).

Table 3.4: Summary of unloaded calibration results.

Serial number	Temperature calibration factor (kPa/°C)		Ratio of temperature calibration factors[2]	Goodness of fit, R^2 (linear)	Maximum pressure variation[3] (kPa)	Percentage of cell's full-scale range[4] (%)
	Manufacturer	Laboratory[1]				
Field contact pressure cells						
26158	-0.2071	-0.2077	1.0029	0.9978	7.6	2.2
26159	-0.1324	-0.1949	1.4721	0.9977	7.1	2.0
26886	0.0479	-0.0729	-1.5219	0.9679	2.9	0.4
26888	0.0280	-0.1056	-3.7714	0.9797	4.0	0.6
25612	0.0471	0.0204	0.4331	0.7218	1.1	0.1
25613	-0.0458	-0.0714	1.5590	0.9773	2.7	0.3
Contact pressure cell						
04-7935	-0.08522	-0.1572	1.8446	0.9933	6.5	1.9
Earth pressure cell						
05-8284	-0.0908	-0.1302	1.4339	0.9753	5.3	0.8

[1]Temperature calibration factor found by fitting a linear equation through the unloaded test data.
[2]Ratio of the laboratory calibration factor to the manufacturer's calibration factor.
[3]Maximum absolute uncorrected pressure variation over the total test temperature range.
[4]The percentage of the cell's full-scale range that the maximum pressure variation represents.

3.3.12 Calibration Tests of Loaded Cells

A metal pressure chamber was needed for the loaded test in the temperature control room (Figure 3.16). Since the chamber was too small to test more than one pressure cell at a time, only one was possible. Figure 3.17 shows that the pressure cell was positioned halfway up the box and enclosed in sand to represent field conditions. Two thermocouples were installed on either side to check if the chamber's interior had gotten accustomed to the selected temperature level. Lastly, an air bladder was put into the chamber, and a steel cover was attached with bolts.

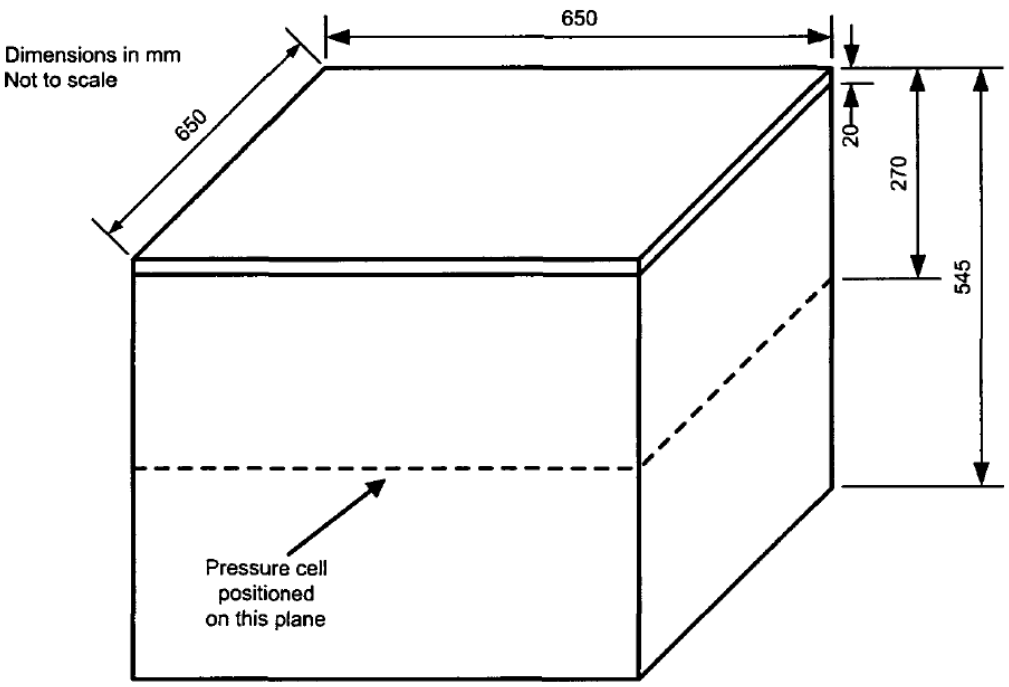

Figure 3.16: Metal pressure chamber used to calibrate contact and earth pressure cells (Huntley and Valsangkar, 2013).

Figure 3.17: Pressure cell positioned in the pressure chamber (Huntley and Valsangkar, 2013).

Upon installing the pressure cell, the environment was adjusted to the appropriate temperature, and the room and pressure cell were permitted to acclimate. Because of the air circulating in the environment room, the pressure cell was no longer directly in touch with the air; this process took more extended than the unloaded tests. In the next step, an air regulator was used to put pressure increments of 68.9 kPa (10 lb/in2) to the cells. A contact earth pressure cell operates between 0 kPa and 344.7 kPa (50 lb/in2), while earth pressure cells operate between 0 kPa and 413.7 kPa (60 lb/in2). Even though side friction would result during loading, it was considered insignificant compared to applied pressure. Finally, data were gathered at each pressure increment. Three loading cycles were run at each temperature level, with the data showed later being an average of these three cycles.

Table 3.5: Summary of loaded contact and earth pressure cells results.

Applied pressure (kPa)	Maximum pressure variation over the test temperature range[1] (kPa)			
	Contact pressure cell #04-7935		Earth pressure cell #05-8284	
	Uncorrected	Laboratory[2]	Uncorrected	Laboratory[2]
0	9.8 (2.8)	3.1 (0.9)	6.0 (0.9)	2.2 (0.3)
68.9	28.7 (8.2)	22.0 (6.3)	7.3 (1.0)	4.4 (0.6)
137.9	37.3 (10.7)	30.7 (8.8)	12.2 (1.7)	7.5 (1.1)
206.8	42.7 (12.2)	36.1 (10.3)	18.0 (2.6)	12.8 (1.8)
275.8	45.0 (12.9)	38.4 (11.0)	24.3 (3.5)	19.0 (2.7)
344.7	44.4 (12.7)	37.7 (10.8)	30.4 (4.3)	25.1 (3.6)
413.7	N/A	N/A	36.3 (5.2)	31.0 (4.4)

[1]This is the maximum absolute pressure variation over the test temperature range of ~ 40°C. The number in parenthesis is the percentage of the cell's full-scale range that the maximum pressure variation represents.
[2]Values from test data corrected using the linear thermal correction factors found from the unloaded tests.

3.3.13 Environment Canada Weather Data

Environment Canada (2002), situated at a monitoring airport about 15 km from the instrumented bridge, provided the study site's weather data. The temperature profile for the study location was made from ambient temperatures every hour. Data from the installed instruments were used to plot this profile and assess the thermal response of the bridge. Environment Canada (2002) also provided barometric pressure data, which applied barometric pressure rectification to the contact earth-pressure-cell data. Interpolation of the barometric pressures between each hour was carried out to obtain a value correlating each pressure data readings.

Table 3.6: Temperature maxima and minima during the study period (Huntley, 2009).

Year	Weekly minimum temperature[1]		Weekly maximum temperature[1]	
	Week	(°C)	Week	(°C)
2004	Dec 26 – Jan 1	-9.2	n/a[2]	n/a[2]
2005	Jan 23 – Jan 29	-16.5	Jul 17 – Jul 23	22.7
2006	Feb 26 – Mar 4	-11.5	Jul 16 – Jul 22	21.9
2007	Feb 4 – Feb 10	-15.2	Jul 22 – Jul 28	23.1

[1]The temperatures given were averaged over the selected week.
[2]The initial date selected was October 20, 2004. Thus, a true maximum temperature was not obtained as data was not being collected during the typical time that this maximum temperature would occur.

The four different types of days that have been chosen for daily bridge response review are pointed out in Table 3.7. Clear and cloudy dates were chosen to display the various solar radiations and ambient temperatures in the summer and winter. According to Lawver (1998), bridges are heated and cooled by the air surrounding them and, to a significant degree, by the solar radiation observed at deck level in summer. The study showed that ambient and deck temperatures lagged solar radiation, so a lag in bridge behaviour is also expected. Also, Lawver (1998) concluded that the bridge structure is heated and cooled by the air surrounding it in the winter, in contrast to solar

radiation, which had little impact due to the earth's tilt. Thus, the bridge should react faster to temperature fluctuations than during the summer.

Table 3.7: Days selected for assessment of daily bridge behaviour (Huntley, 2009).

Date	Temperature range (°C)	Average temperature (°C)	Weather description
January 11 2005	-12.9 to -1.7	-8.8	Clear day
January 17 2005	-14.9 to -8.2	-11.1	Cloudy day
July 16 2005	11.0 to 28.7	20.2	Clear day
July 27 2005	17.6 to 27.7	21.8	Cloudy day

3.3.14 Abutment Movements

In order for an integral bridge to perform well, abutment movements must be carefully investigated. From previous sections, integral abutments accommodate thermal fluctuations by rotating and translating. In order to measure these movements, tilt meters and deformation meters were used simultaneously.

3.3.14.1 Tilt Meters

At each abutment, tilt meters were mounted to measure the rotation (Figure 3.5). A positive change in rotation shows that the abutment walls rotate into the backfill and away from the centre pier, as expected during warmer temperatures. Similarly, a negative change in rotation shows that the abutment walls rotate away from the backfill and towards the centre pier, foreseen during cooler temperatures. Figures 3.18 and 3.19 illustrate how the east and west abutments have rotated and the temperature profile over the same period. Also, the rotation and ambient temperature averages for each week were estimated.

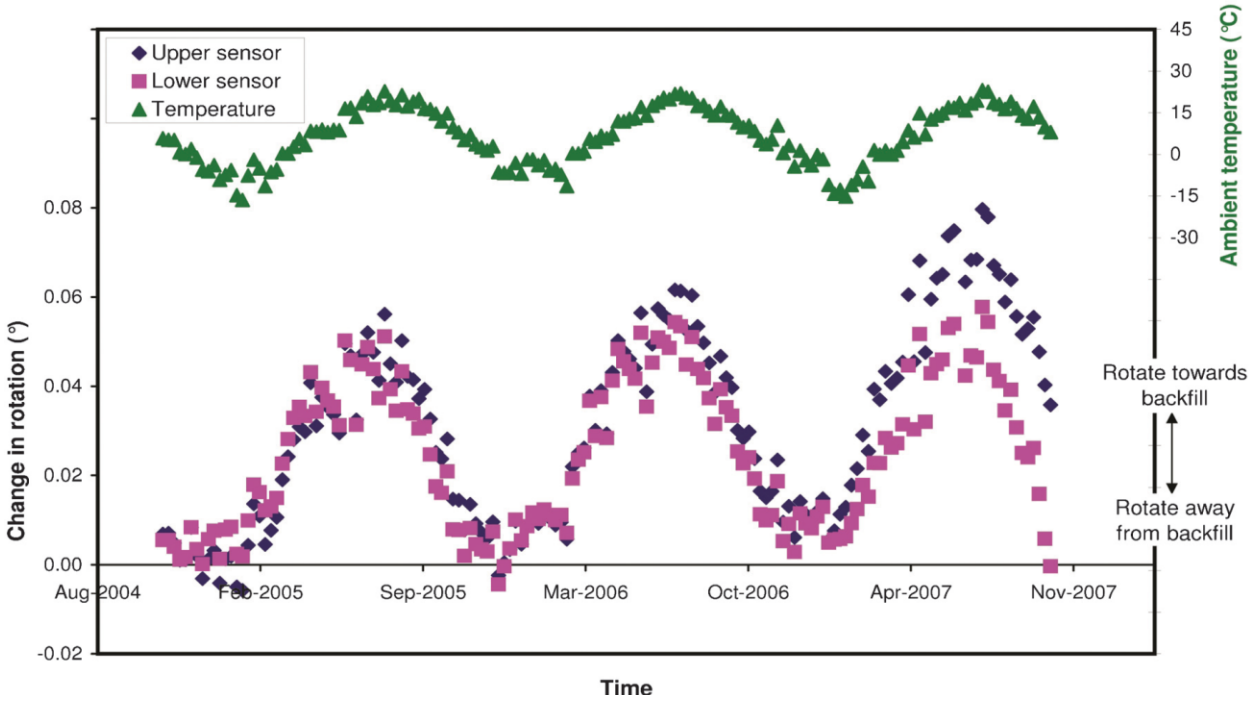

Figure 3.18: East abutment rotation and ambient temperature profile (Huntley and Valsangkar, 2013).

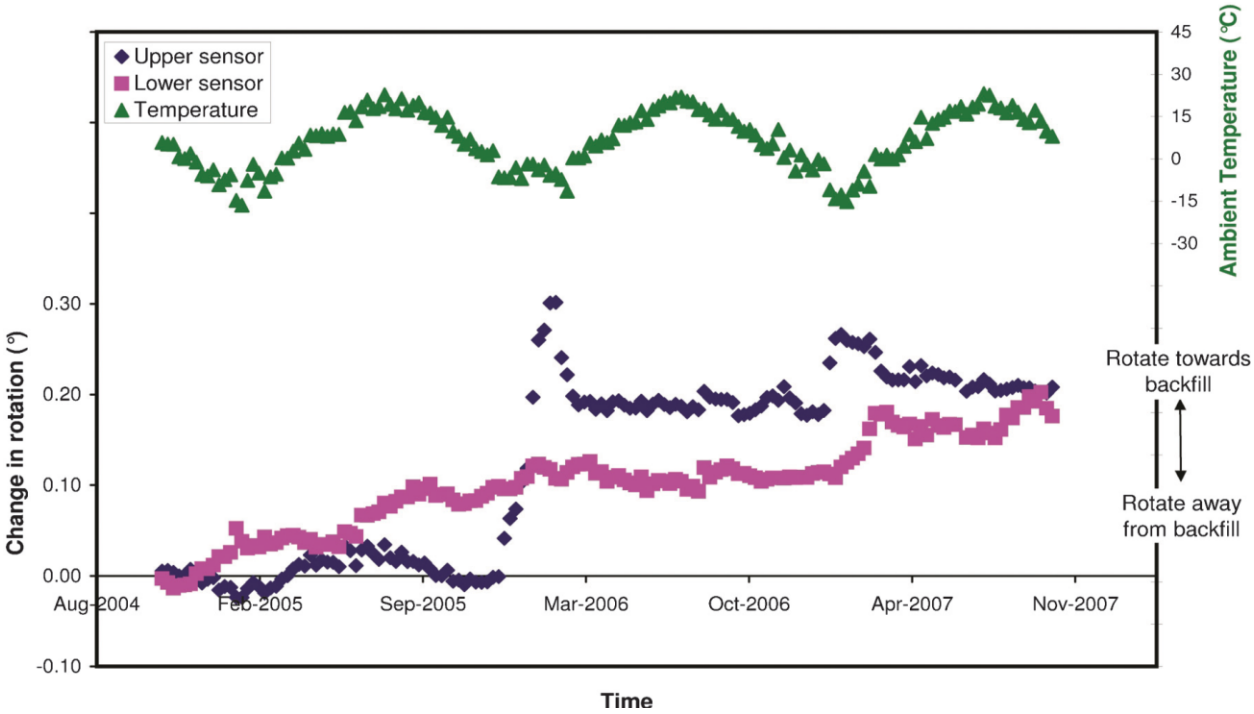

Figure 3.19: West abutment rotation and ambient temperature profile (Huntley and Valsangkar, 2013).

Table 3.8 shows the maximum rotational change for the east abutment over each year. Data on the west abutment is not revealed since its validity is unsure.

Table 3.8: Maximum variations in abutment rotation during the study period (Huntley, 2009).

Year	Rotation variation[1] (°)		Avg. rotation variation (°)
	Upper	Lower	
East abutment			
1	0.06	0.05	0.06
2	0.06	0.06	0.06
3	0.07	0.06	0.07

[1]The maximum variations were determined from weekly averaged data.

3.3.14.2 Deformation Meters

Deformation meters were mounted at each abutment to measure the lateral translation (Figure 3.6). A positive change in translation shows that the abutment walls are moving away from the backfill and towards the centre pier, as anticipated in colder temperatures. Correspondingly, a negative change in the translation shows that the abutment walls move towards the backfill and away from the centre pier, as expected during warmer temperatures. Figures 3.20 and 3.21 illustrate how the east and west abutments have translated and the temperature profile over the same period. Also, the translation and ambient temperature averages for each week were estimated.

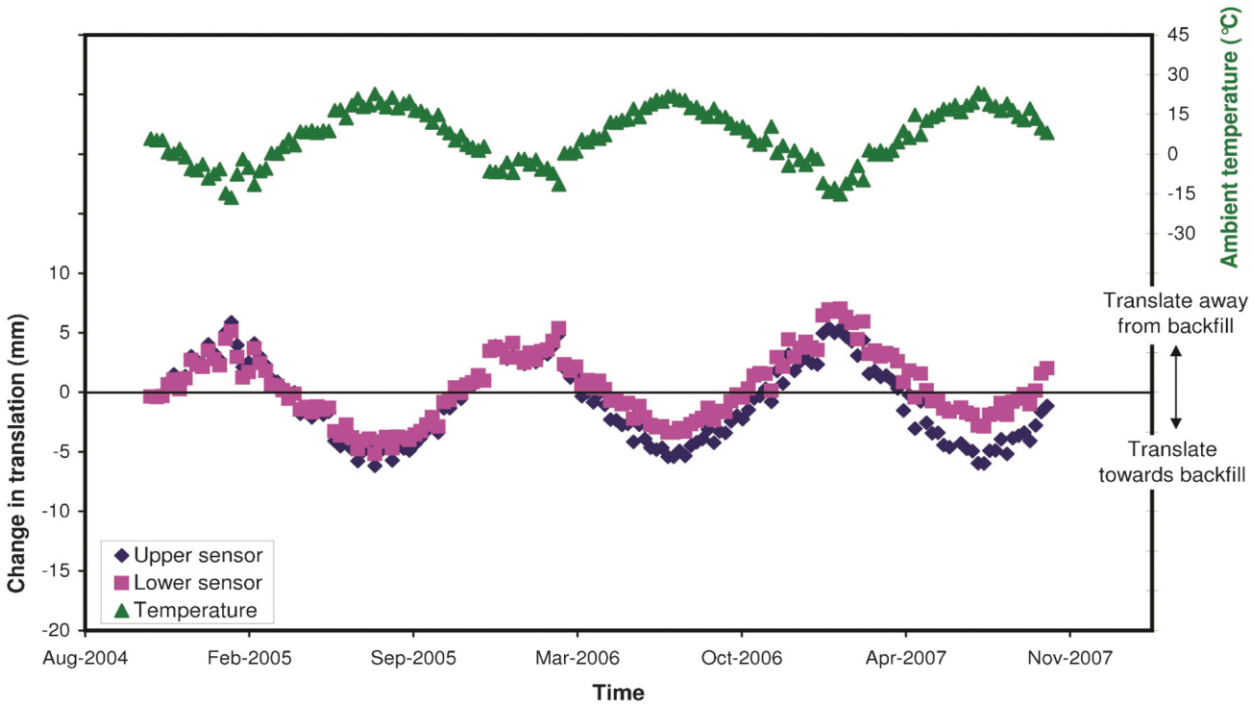

Figure 3.20: East abutment translation and ambient temperature profile (Huntley and Valsangkar, 2013).

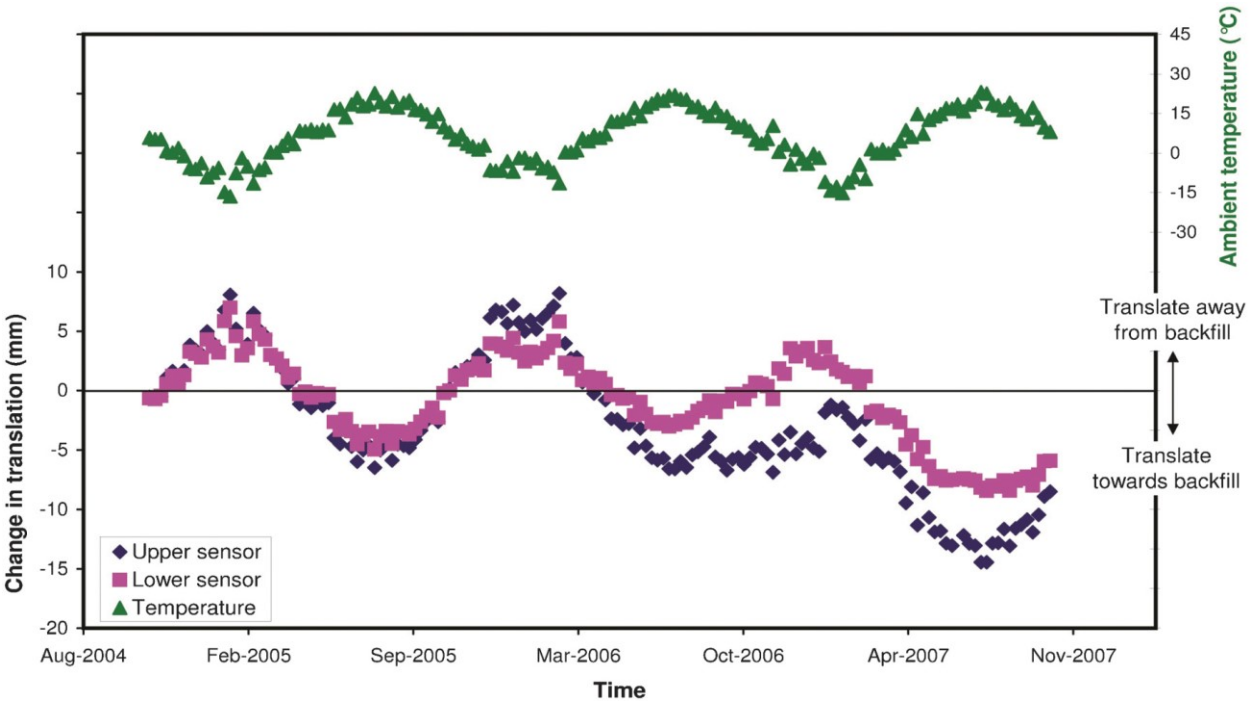

Figure 3.21: West abutment translation and ambient temperature profile (Huntley and Valsangkar, 2013).

Table 3.9 lists the maximum translation change for the east abutment and west abutment over each year. On average, the west abutment experienced more translation than the east abutment.

Table 3.9: Maximum variations in abutment translation during the study period (Huntley, 2009).

Year	Translation variation[1] (mm)		Avg. translation variation (mm)
	Upper	Lower	
East abutment			
1	12.1	10.3	11.2
2	10.3	8.8	9.6
3	11.4	9.9	10.7
West abutment			
1	14.6	12.0	13.3
2	14.8	8.8	11.8
3	13.3	12.1	12.7

[1]The maximum variations were determined from weekly averaged data.

3.3.15 Seasonal Abutment Movement Conclusions

In this study, the annual maximum change in rotation and translation of east abutments was 0.06° and 10.5 mm, respectively. Based on the data, the east abutment's translation and rotation exhibited similar responses to ambient temperature changes over the study period.

Generally, there was a little more movement on the west abutment than on the east abutment. It is believed that variations in sun exposure or compaction of the backfill materials could have led to this difference. Further, the superstructure was mainly adapted to thermal expansion and contraction via an abutment translation rather than through rotation. With this kind

of movement, the abutment foundation piles are more likely to bend into a double curvature than a single curvature, as predicted with abutment rotation (Figure 3.22).

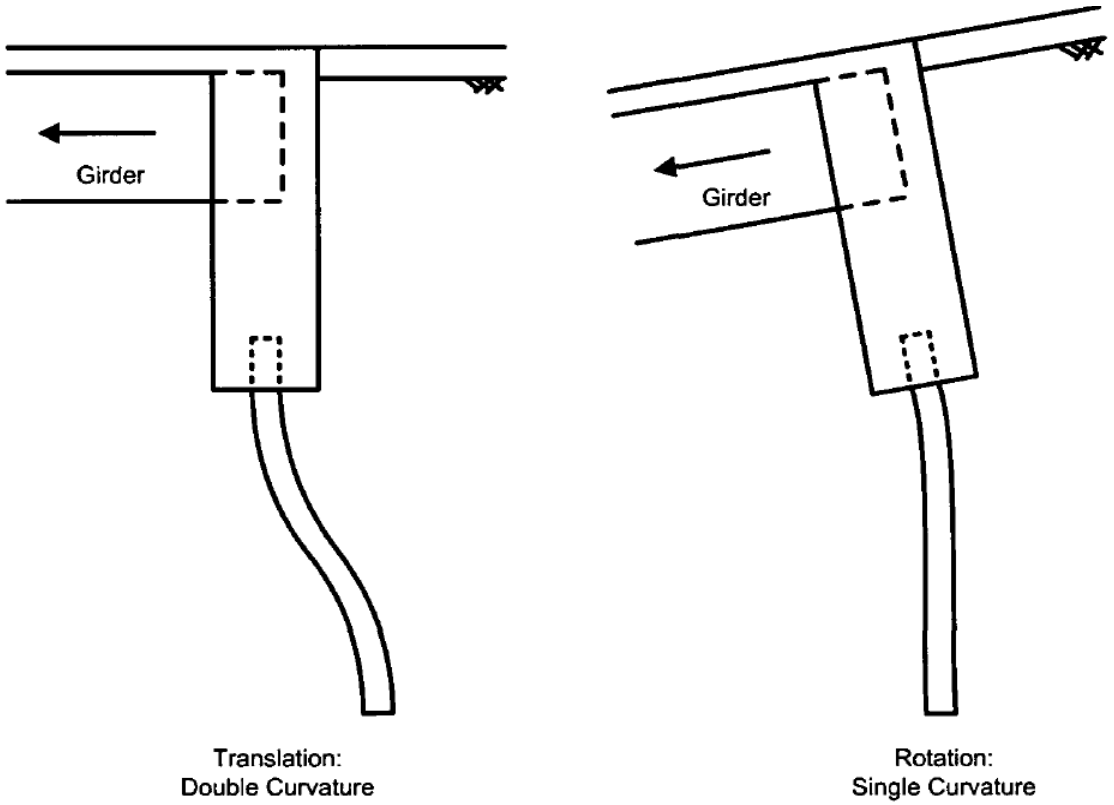

Figure 3.22: Thermal abutment movements and the effect on the foundation piles (Huntley, 2009).

3.3.16 Earth Pressures Acting on the Abutment

3.3.16.1 Pressure Cells

When the abutment walls displace to accommodate the superstructure's thermal response, they cause earth pressures to develop behind them. Based on these pressures, the thickness of abutment walls and reinforcement requirements are designed. Figure 3.7 depicts the pressure

profile acting on abutment walls during the study period based on data obtained from contact pressure cells in the field.

A positive change in the pressure shows that the abutment walls are moving towards the backfill. In contrast, a negative change in the pressure means the abutment walls are moving away from the backfill. Figures 3.23 and 3.24 illustrate the shift in earth pressures acting on the east and west abutments over time and the study period's ambient temperature profile. Weekly averages for the pressure and ambient temperature data were also estimated.

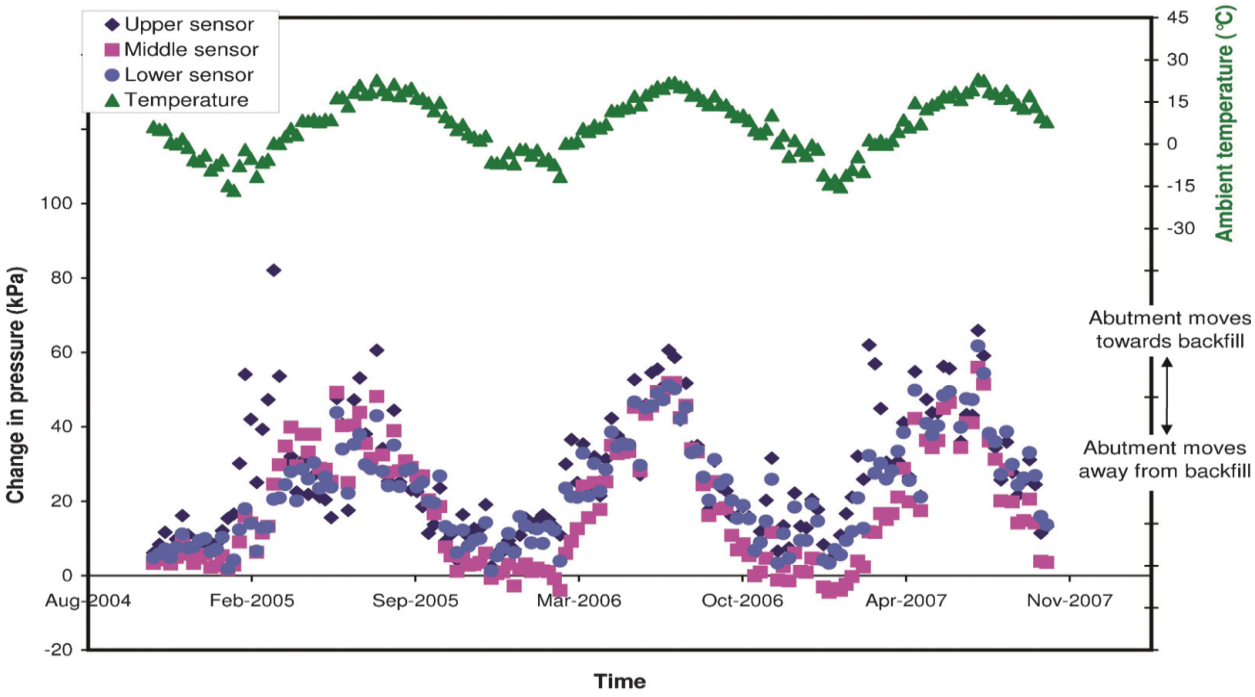

Figure 3.23: East abutment pressure variation and ambient temperature profile (Huntley and Valsangkar, 2013).

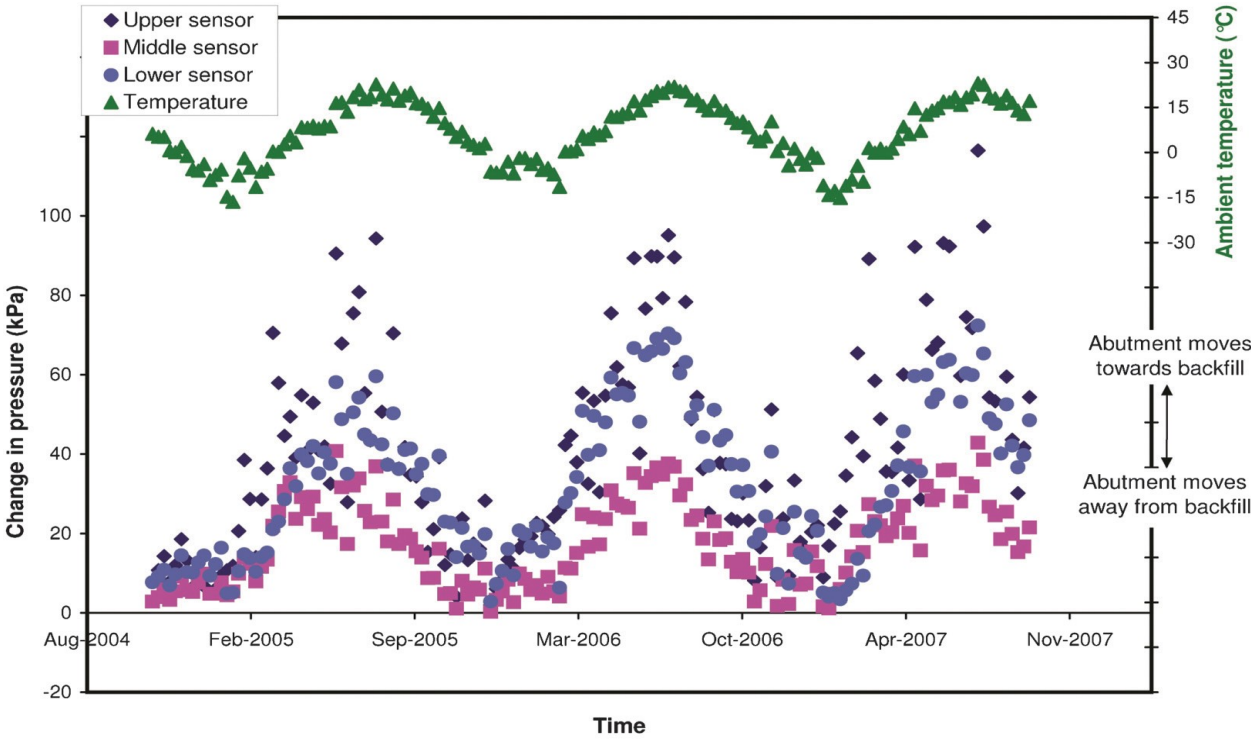

Figure 3.24: West abutment pressure variation and ambient temperature profile (Huntley and Valsangkar, 2013).

The maximum variations in earth pressure within each study year are indicated in Table 3.10, both for the east and west abutments. The upper sensors provided more significant pressure variations on the east abutment, and the lower sensors exhibited smaller variations as depth increased, although overall, the variations in these three sensors were alike. Similarly, variations along the west abutments were characterized by close patterns, except that the middle sensor had the lowest pressure variation. A limitation in distributing the pressure at this sensor resulted in its estimation being lower than the applied pressure.

Table 3.10: Maximum variations in earth pressure acting on the integral abutments during the study period (Huntley, 2009).

Year	Earth pressure variation[1,2] (kPa)					
	East abutment			West abutment		
	Upper	Middle	Lower	Upper	Middle	Lower
1	55.2	47.5	42.0	89.3	37.9	54.7
2	58.2	55.9	49.8	93.1	37.4	67.6
3	62.5	60.4	58.4	108.3	41.7	69.0

[1]The maximum variations were determined from weekly averaged data.
[2]A summer value was selected over the higher March 2005 value as it is suspected this spike in pressure change in the winter is due to water seeping into the backfill and freezing.

3.3.17 Seasonal Earth Pressure Conclusions

After the research, Huntley (2009) concluded that the maximum annual pressure variation for the east abutment ranged from 50.1 kPa to 58.6 kPa and for the west abutment, it ranged from 39.0 kPa to 96.9 kPa. As stated in the results, the west abutment had more substantial pressure variations than the east abutment, which was not anticipated, as the west abutment encountered a little more displacement than the east abutment.

On the east abutment, earth pressure increased during thermal expansion. On the other hand, earth pressure on the west abutment increased from the first to the second year but reduced by the third year. Nevertheless, data from the deformation meters indicate that the decrease is caused by the data being offset horizontally as the abutment translation has shown less contraction and more expansion in year three than before. In general, the three study years have not yielded a conclusive result concerning the presence of earth pressure ratcheting on this structure. It is also crucial that this structure indicates translation as the primary mode of abutment movement, which negates most research findings.

CHAPTER FOUR

DEVELOPMENT AND VALIDATION OF A TWO-DIMENSIONAL FINITE ELEMENT MODEL

4.1 Introduction

Two finite element models (Mohr-Coulomb and Hardening Soil) were developed to analyze how earth pressures are generated behind the east abutment of the investigated integral bridge in chapter three. The developed models were verified against the measured field data. This chapter will describe each employed soil model and examine their respective effect on the predicted earth pressures due to cyclic loading. Before that, brief background information on soil-structure interaction needs to be outlined, as the aim of this research is to model the soil-structure interaction of an existing Integral Abutment Bridge.

4.2 Background

Since the invention of Integral bridges, problems associated with installation, maintenance, repair and replacement of expansion joints and end bearings have been curbed significantly. However, these bridges have left engineers with several research gaps that need to be filled over time. One of these unsolved problems solely concentrates on the soil-structure interaction of these structures. Experiments have proven that abutments' cyclic displacement may cause a significant amount of strain ratcheting in the backfill materials. These movements can also deteriorate the

bridge end's serviceability by creating settlements behind the abutment (England and Tsang, 2001). As a result, developing a numerical model that can efficiently analyze and predict integral abutment bridges' soil-structure interaction is necessary.

4.3 Description of The Soil Models

4.3.1 Mohr-Coulomb Soil Model

When soil is subjected to load within its yield limit, it follows Hooke's linear elasticity law. Coulomb's law of perfect plasticity then governs soil's behaviour under further load beyond its elastic limit. Combining Hooke and Coulomb's law, a generalized formulation in a plasticity framework gives us a constitutive soil model known as the Mohr-Coulomb model. Mohr-Coulomb's model can be considered a first-order approximation of actual soil behaviour (Thevaneyan et al., 2014). This elastic perfectly-plastic model requires five basic input parameters: Young's Modulus, E, Poisson's ratio, ν, Cohesion, c, Friction angle, φ and Dilatancy angle, ψ. This model is well-known, and it is quite simple.

4.3.2 Hardening Soil Model

The hyperbolic Hardening Soil model (Schanz et al. 1999) was first used to model the stress-dependent variation of the soil materials' stiffness due to the abutment's loading directions. Geotechnical engineers appreciate the hyperbolic hardening soil model due to its controllable soil behaviour analysis using two stiffness parameters. It is a modification of the Duncan and Chang (1970) hyperbolic model. This advanced soil model is different from the elastic-perfectly plastic

Mohr-coulomb soil model because the former uses the plasticity theory while the latter follows the theory of elasticity. The Hardening Soil model also considers the utility of yield cap surface and accounts for soils' dilatancy. Its basic parameters are Young's modulus for primary loading, E_{50}, Young's modulus for unloading/reloading, E_{ur}, Oedometer Stiffness, E_{oed}, Cohesion, c, a Friction angle, φ and Dilatancy angle, ψ.

4.4 Development of Finite Element Models

The finite element software selected for this research is PLAXIS 2D. The leading geotechnical finite element software was developed specifically for the deformation analysis of soils and substructural members. It is renowned for ease of use and accuracy, and it assists with optimizing designs more effectively than applying traditional conservative calculation methods. This software is divided into five tab sheets/modes: Soil, Structures, Mesh, Flow conditions and Staged construction. The modelling process is completed in these five modes. However, the flow conditions mode is skipped, as it is not needed for this analysis. The development of the finite element models under each tab sheet is further explained in this section.

4.4.1 Project Properties

The project title and the basic parameters of the finite element models were set in this window. The 15-nodded cubic strain triangular elements were used at plane strain conditions. The lateral boundaries were placed about three times the structure's width in each direction to simulate the infinite medium, and the bottom boundary was set at 30m below the ground surface.

4.4.2 Soil Mode

Each soil and concrete materials model and parameters are taken from Huntley's Ph.D. research in 2009 are first defined in this mode/tab sheet. The borehole feature in this mode defined the soil stratigraphy, general water levels, and the soil layers' initial conditions. The Crushed stone, Borrow A, Clayey sand, and Mudstone materials were assigned to their designated layer, and the water level is below the entire profile. The different soil properties in the first FE-Model using the Mohr-Coulomb Soil Model are shown in Table 4.1, while Table 4.2 shows the soil properties for the Hardening Soil Model.

Table 4.1: The soil parameters using the Mohr-Coulomb soil model (Huntley, 2009).

Material	**Ø ^{0}**	**C (Kpa)**	**E (Mpa)**	**ɣ (K.N./m^{3})**
Crushed stone	36	0	90	20
Borrow A	34	29	40	21.7
Drainage Layer	31	0	35	18
Clayey sand	35	20	60	19
Mud-stone	36	0	120	20
Loose Sand	30	0	20	16

Table 4.2: The soil parameters using the Hardening soil model (Huntley, 2009).

Material	Ø°	C (Kpa)	E50 (Mpa)	Eode (Mpa)	Eur (Mpa)	ɣ (K.N./m^3)
Crushed stone	36	0	90	80	270	20
Borrow A	34	29	40	32	120	21.7
Drainage-Layer	31	0	35	28	105	18
Clayey sand	35	20	60	48	180	19
Mud-stone	36	0	120	96	320	20
Loose Sand	30	0	20	16	60	16

4.4.3 Structures Mode

Geometric entities, structural elements and boundary conditions are defined in this mode. The geometric entities are the physical model's essential components, and features such as structures, loads, displacements, etcetera can be assigned to them.

The polygon feature in this mode was used to create the soil clusters, such as; the concrete elements (abutment and approach slab), the loose sand trench and the drainage material layer. The reinforced concrete abutment and approach slab was modelled using the elastic model shown in Table 4.3. The field's H-steel beam dimensions (I=93.7x10-6, A=16.7x10-3) were used to simulate the H-piles' rows as plate elements in the models. The piles' structural properties and internal spacing (1160mm) copied the same configuration as the field case study. Interfaces were defined at all soil-structure meeting points.

The backfilling works with drainage and borrow A materials were simulated by horizontal lines across the model at every 300mm thickness. The field's excavation slope at 1V:2H in the

traffic direction was mimicked by drawing a diagonal line from the abutment's outer face to its bottom end. Finally, the bridge deck's axial load was calculated and applied as a line load at the abutment's top. The used piles' parameters in the finite element models are shown in Table 4.4.

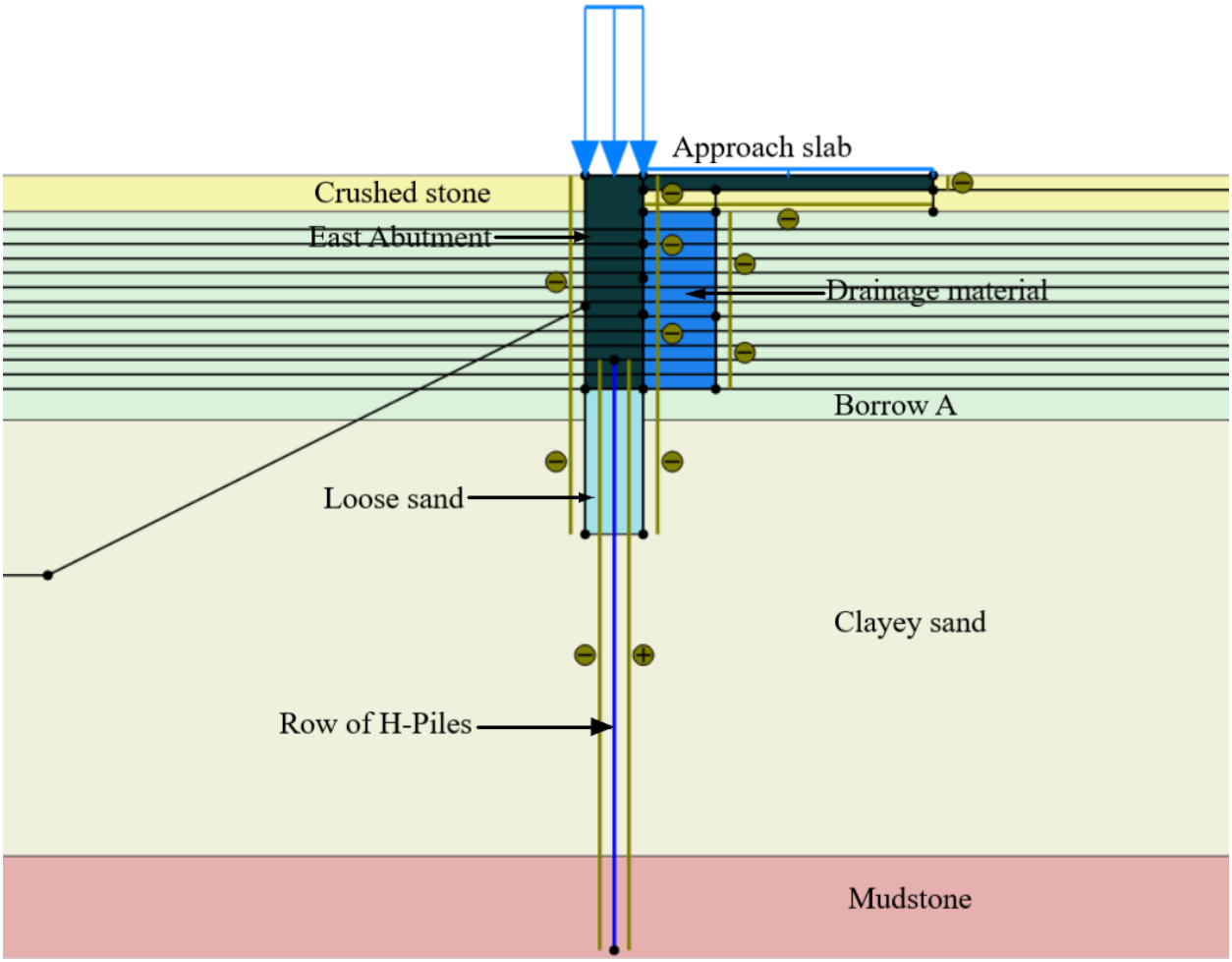

Figure 4.1: Geometric entities of the east abutment in the structures tab sheet.

Table 4.3: The elastic model parameters for the concrete (Huntley, 2009).

Material	E (Mpa)	ɣ (K.N./m^3)	υ (poisons ratio)
Concrete	31000	24	0.15

Table 4.4: The used parameters of H-steel piles (Huntley, 2009).

Material	E.I. (K.N./m^3)	E.A. (KN/m)	υ (poisons ratio)
Pile	16.20x10^3	2.88x10^6	0.30

4.4.4 Mesh Generation Mode

After the full definition of the structural and soil geometry, the next step is to divide the geometries into finite elements to perform finite element calculations. This composition of finite elements is called a mesh, which is created in this mode.

The **mesh options** window (Figure 4.2) gives the option to define the general mesh properties, and the medium option was selected as the mesh's element distribution for these analyses. The mesh generation process takes into account the soil stratigraphy and structural objects, loads and boundary conditions. The concluded mesh used for these analyses is shown in Figure 4.3.

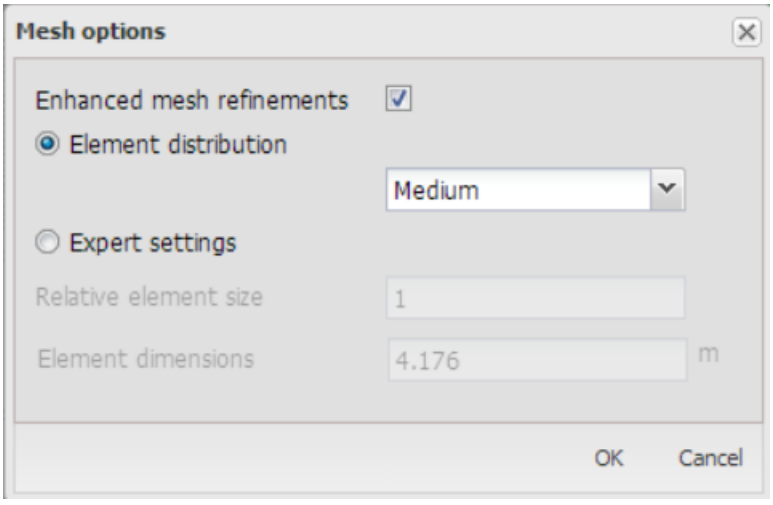

Figure 4.2: *Mesh options* window with the medium element distribution selected for calculations.

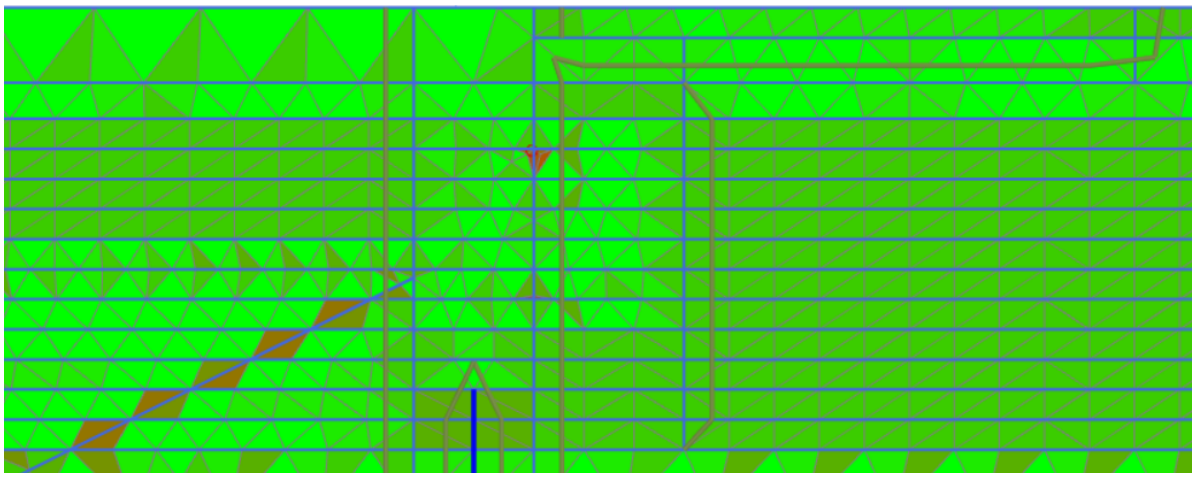

Figure 4.3: Generated mesh quality for the finite element calculations.

4.4.5 Staged Construction Mode

The construction procedure and interface stress calculations for the case study were simulated in the staged construction tab. To simulate a construction process, soil clusters can be activated and deactivated; hence, a realistic analysis is achievable. The boundary conditions to the models are set in this mode before calculations. The lateral boundaries were normally fixed in the horizontal direction, the top boundary is free for ease of abutment displacement, and the bottom is fully fixed. Each stage with respective figures is listed as follows, and they are represented as phases on PLAXIS.

4.4.5.1 Initial Phase

The K_o procedure calculation type in Plaxis was used to simulate the initial in-situ stress in which the initial geostatic stress was established, assuming increasing vertical stress with depth.

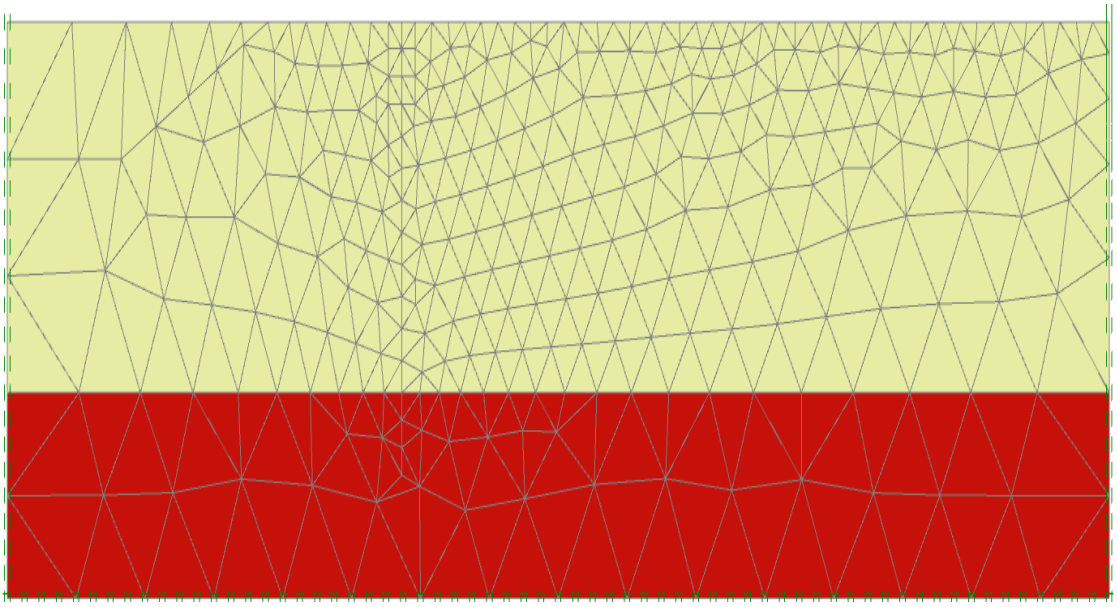

Figure 4.4: Initial in-situ K_o stresses.

4.4.5.2 Excavation Phase

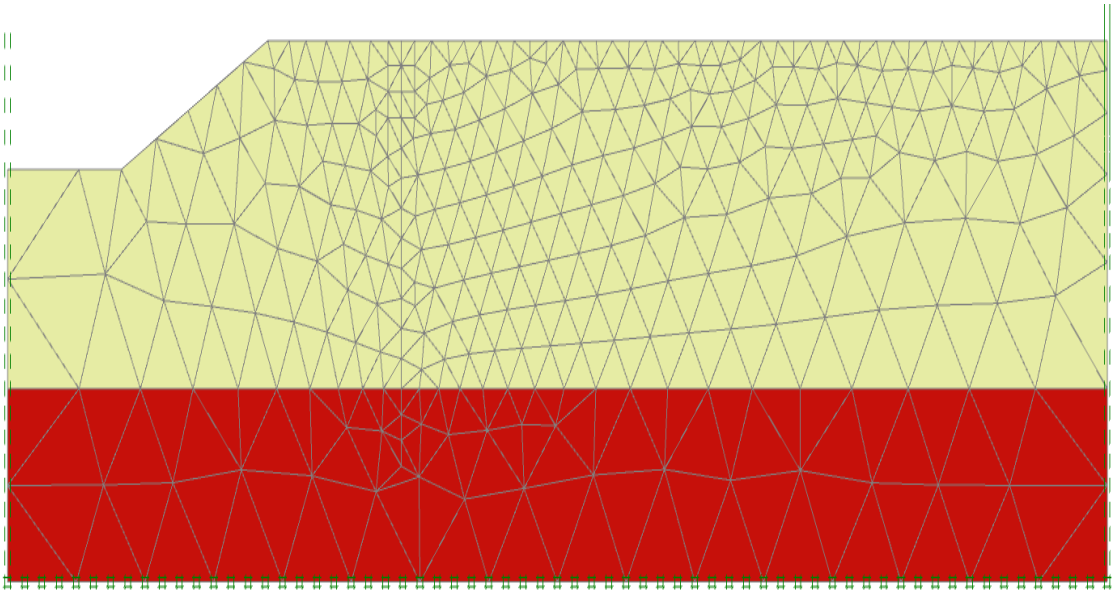

Figure 4.5: The excavation works for the watercourse.

4.4.5.3 Pile Platform Phase

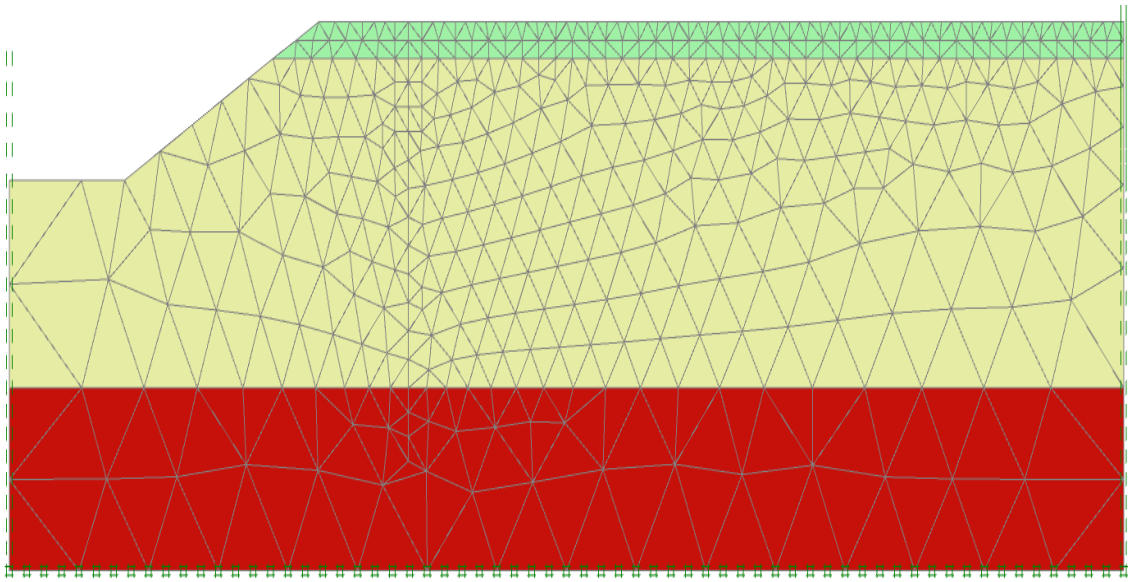

Figure 4.6: Activate the backfilling lifts beneath the abutment.

4.4.5.4 Loose Sand and Pile Installation Phase

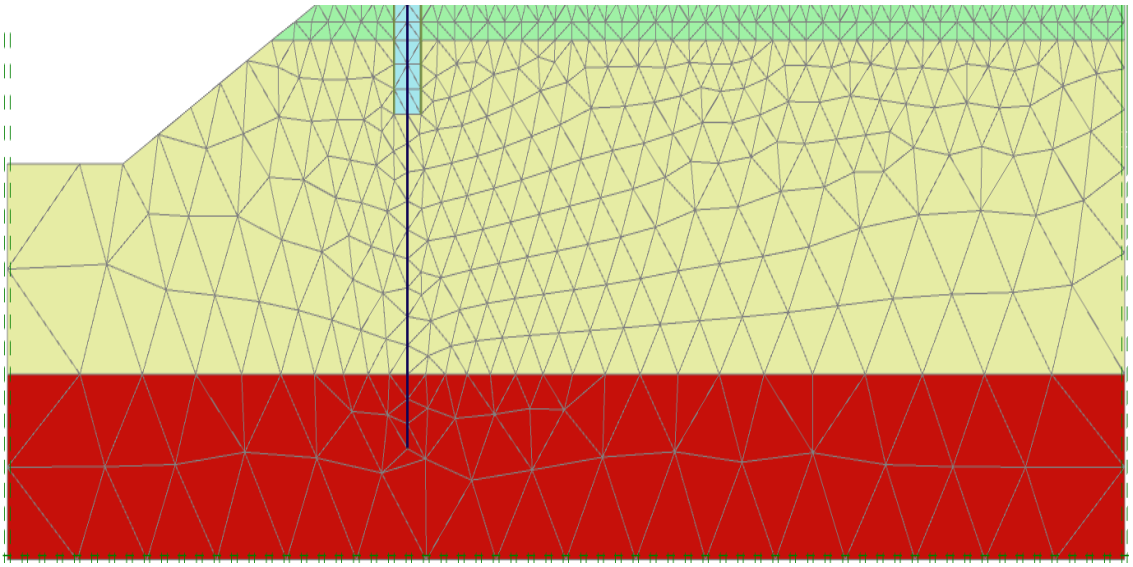

Figure 4.7: Installation of steel pile works and the loose sand trench of 1200mm width.

4.4.5.5 Abutment Construction Phase

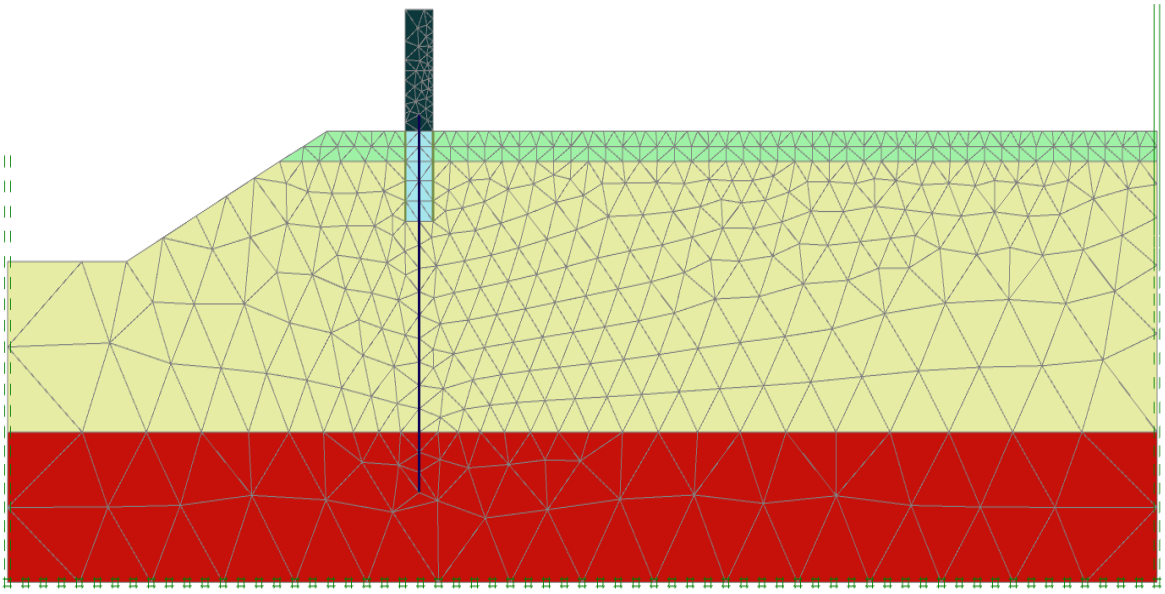

Figure 4.8: Completing the concrete abutment's construction works until the finishing level.

4.4.5.6 Backfilling Works (Phase 5 to Phase 16)

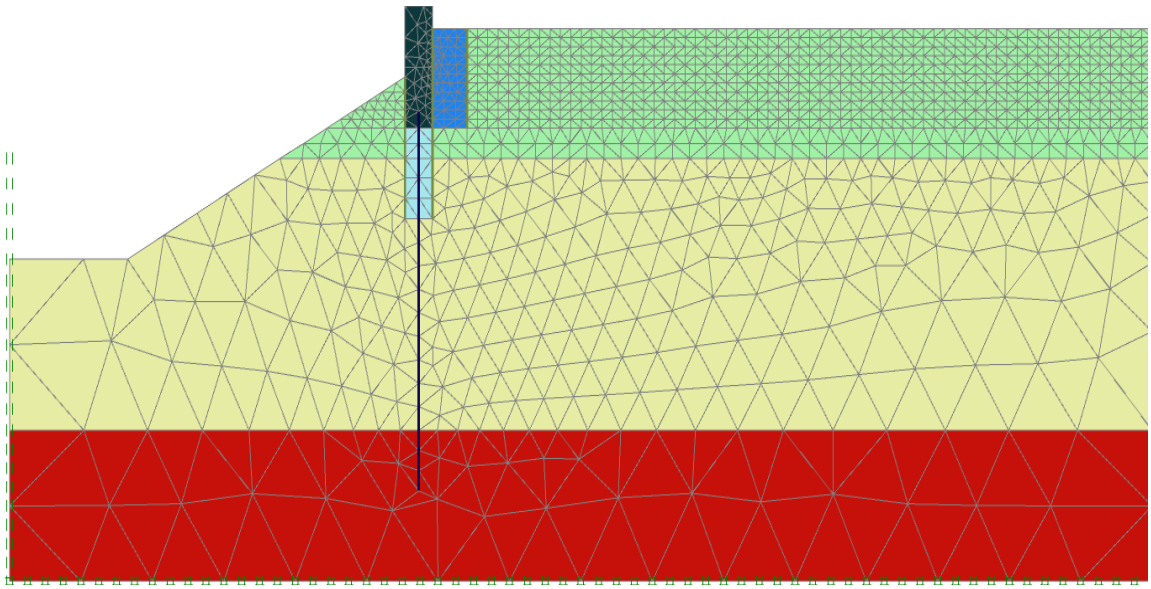

Figure 4.9: Completing the backfilling works behind the abutment until the crushed stone layer's bottom level.

4.4.5.7 Crushed Stone Layer Phase

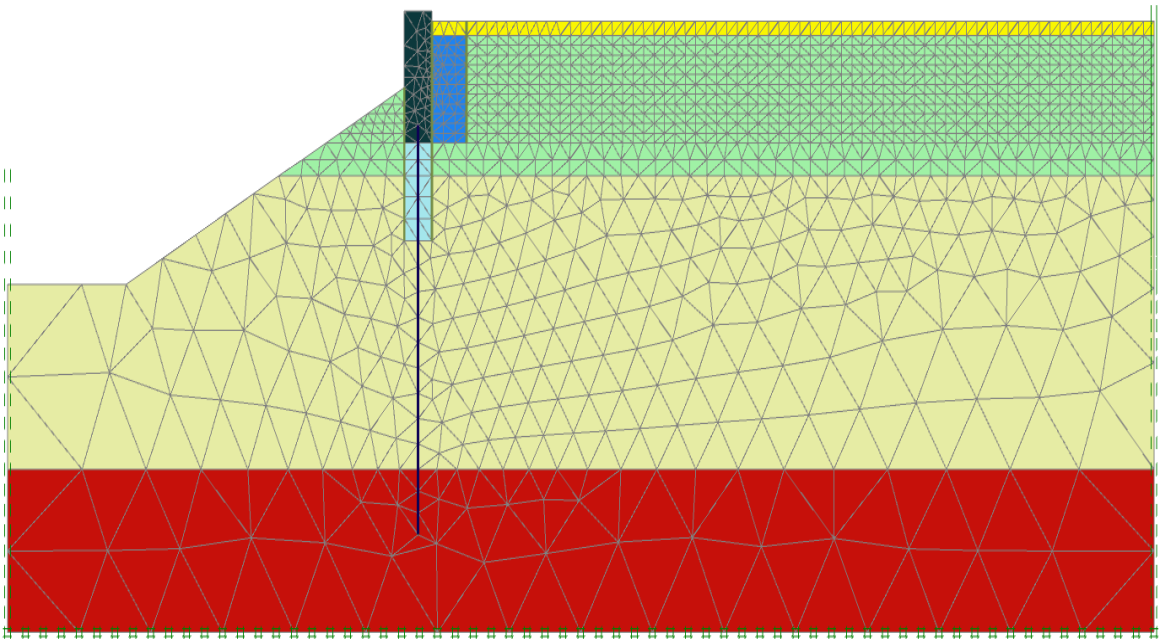

Figure 4.10: Placement of 450 mm crushed stone layer.

4.4.5.8 Approach Slab Phase

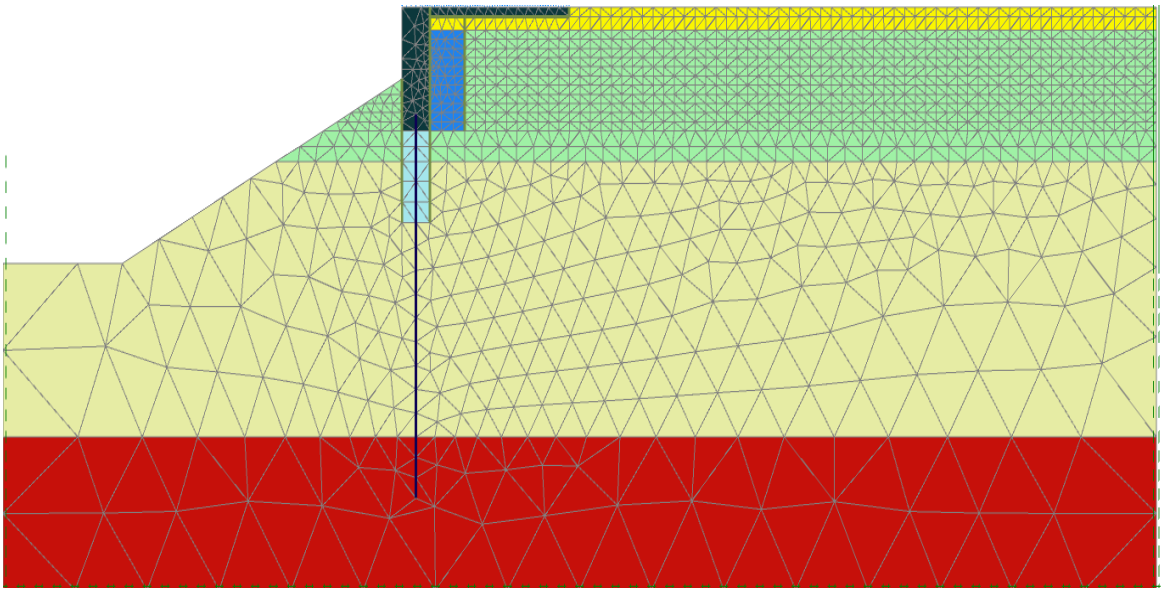

Figure 4.11: Pouring the 300mm thick reinforced concrete approach slab and completing the crushed stone layer.

4.4.5.9 Application of Cyclic Displacements (Phase 19 to 24)

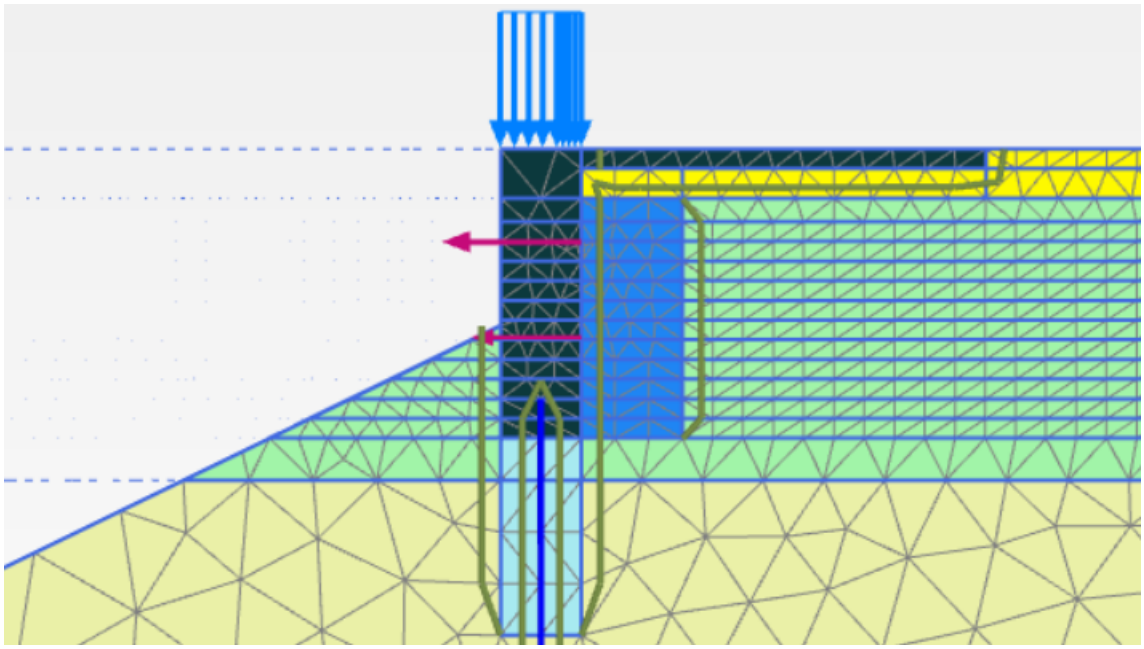

Figure 4.12: Application of the deck load and cyclic displacements due to the effect of the thermal change on the superstructure (Contraction or expansion) on the exact locations of upper and lower transition sensors in the abutment's inner face.

Table 4.5: The average cyclic displacement for different sensors during the three years (Huntley, 2009).

Time	Displacement (mm)		Displacement Direction
	Upper sensor	Lower sensor	
Jan.2005	5.9	5.6	Away from the backfilling
July. 2005	6.2	4.7	Towards the backfilling
Feb. 2006	4.8	3.8	Away from the backfilling
July. 2006	5.5	5.0	Towards the backfilling
Feb. 2007	5.2	5.9	Away from the backfilling
July. 2007	6.2	4.0	Towards the backfilling

4.5 Calibration of The Hardening Soil Model

In numerical modelling, every soil-structure interaction must be simulated by using joint elements called Interfaces. Interfaces can be created next to plates, geogrids or between two soil polygons. The interface properties between the drainage layer, inner abutment surface, borrow A material, crushed stone, and the approach slab were refined to calibrate the finite element model. This calibration was performed by adjusting the interface reduction factor R_{inter} values and the virtual thickness values.

Table 4.6 gives the concluded interface properties at every vital soil-soil and soil-structure interface towards the hardening soil model's final result.

Table 4.6: Calibration data for the Hardening soil model.

Elements	**Interface Type**	**Interface Material**	**Virtual Thickness Factor(s)**	**Interface Reduction Factor, R_{inter}**
Drainage layer / Abutment	Soil-Structure	Drainage layer	0.135 0.300	0.57
Drainage layer / Borrow A	Soil-Soil	Borrow A	0.100 0.550	0.6
Crushed stone / Approach slab	Soil-Structure	Crushed stone	0.100	0.47
Crushed stone / Abutment	Soil-Structure	Crushed stone	0.750	0.47
Borrow A / Abutment	Soil-Structure	Borrow A	0.100	0.6

Other materials such as the Clayey sand, Loose sand and Mudstone have their respective R_{inter} as 0.600, with virtual thickness factors kept at the default value of 0.100. This decision is because they do not influence the interface stress behind the abutment in the model.

4.6 Results and Discussion

This section gives the FE-Models results, including the earth pressure distribution along the abutment's inner face estimated due to the cyclic thermal displacements during the three-year observation period. Each model was compared with the observed field results at the three pressure cells' exact location along the east abutment's inner face. The deformed mesh of the geometries after applying the first-year cyclic displacements is displayed in Figure 4.13.

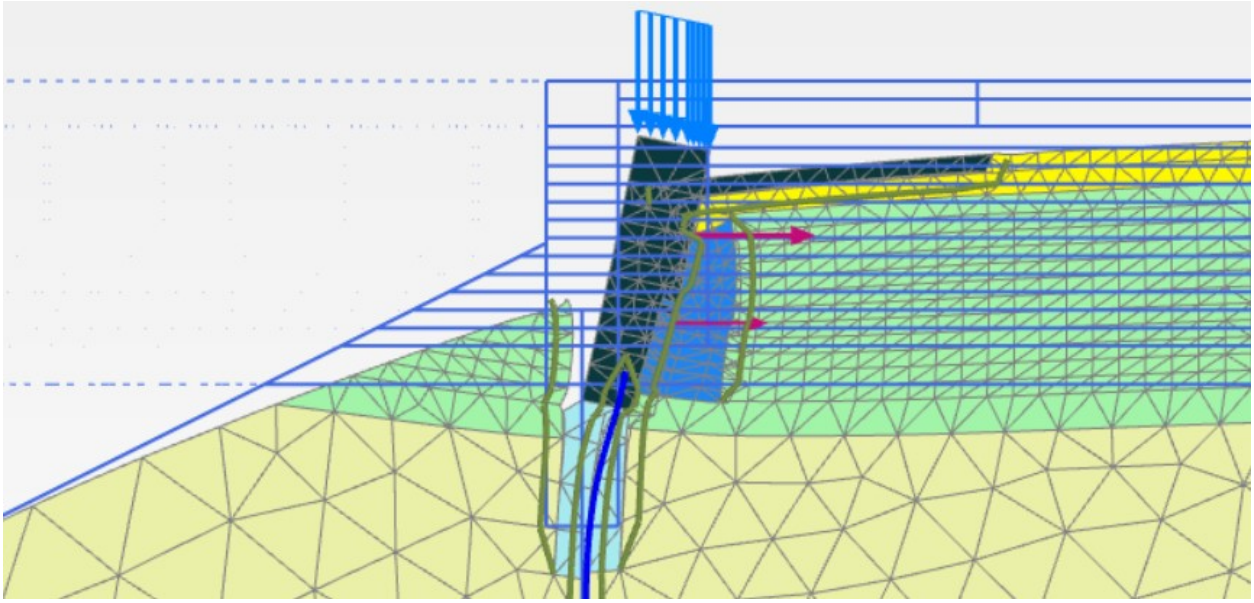

Figure 4.13: The deformed mesh after the first year cyclic displacements in the *Output* window.

As shown in Table 3.7 in Chapter Three, the east abutment field results gave a seasonal variation of 55.2Kpa at the upper observed point and 42 KPa at the lower one. Consecutively, the second year's earth pressure variation in the upper and lower points increases to 58.2 and 49.8 KPa, respectively. Similarly, in the third year, the variation increases to 62.5 and 58.4 KPa.

4.6.1 Mohr-Coulomb Soil Model Results

Table 4.7 shows the variation in earth pressure at the pressure cells' locations using the Mohr-Coulomb Soil model for each study year at the east abutment. While Figure 4.14 compares the earth pressure at the pressure cells' locations and the second FE-Model results using the Mohr-Coulomb Soil model. As a result, Figure 4.15 shows the error percentage in estimating the earth pressure for this soil model.

Table 4.7: Variation in earth pressure at the pressure cells' locations using the Mohr-Coulomb Soil model for each study year.

	Upper	Middle	Lower
Year 1	44.6	44.5	37.1
Year 2	44.2	39.9	30.7
Year 3	39	44.6	36.2

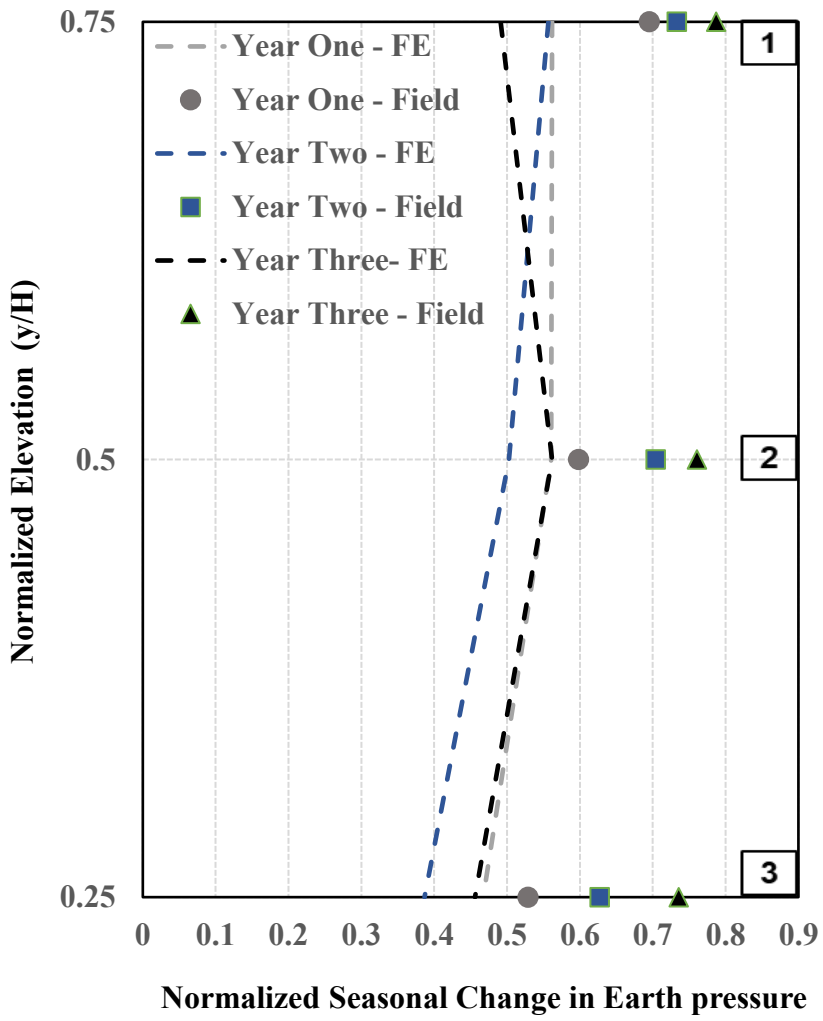

Figure 4.14: Comparing the observed Field earth pressure and the FE-model results using the Mohr-Coulomb Soil Model.

This Mohr-Coulomb soil model percentage error (%) varies from 19.2% to 37.6% for point 1, 6.3% to 26.2% for point 2 and 11.7% to 38% for point 3, as shown in Figure 4.21.

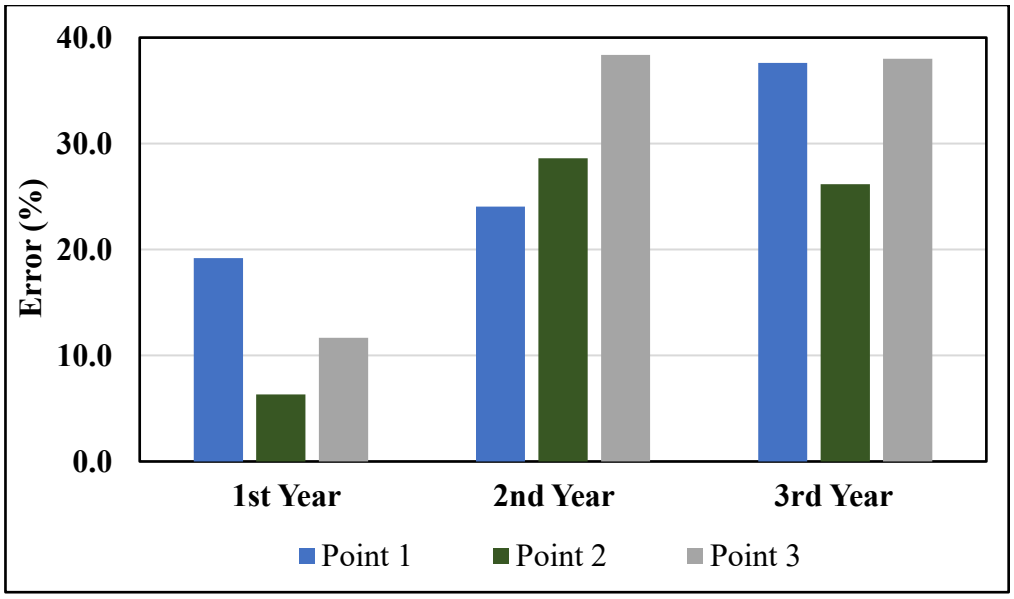

Figure 4.15: The error (%) in estimating earth pressure in the second FE-Model using the Mohr-Coulomb Soil model.

4.6.2 Hardening Soil Model Results

Table 4.8 shows the variation in earth pressure at the pressure cells' locations using the Hardening Soil model for each study year at the east abutment. While Figure 4.16 compares the earth pressure at the pressure cells' locations and the first FE-Model results using the Hardening Soil model. Consequently, Figure 4.17 shows the error percentage in estimating the earth pressure for this soil model.

Table 4.8: Variation in earth pressure at the pressure cells' locations using the Hardening Soil model for each study year.

	Upper	**Middle**	**Lower**
Year 1	55.8	47.9	46.7
Year 2	57.7	55.6	45.9
Year 3	61.9	59.8	51.9

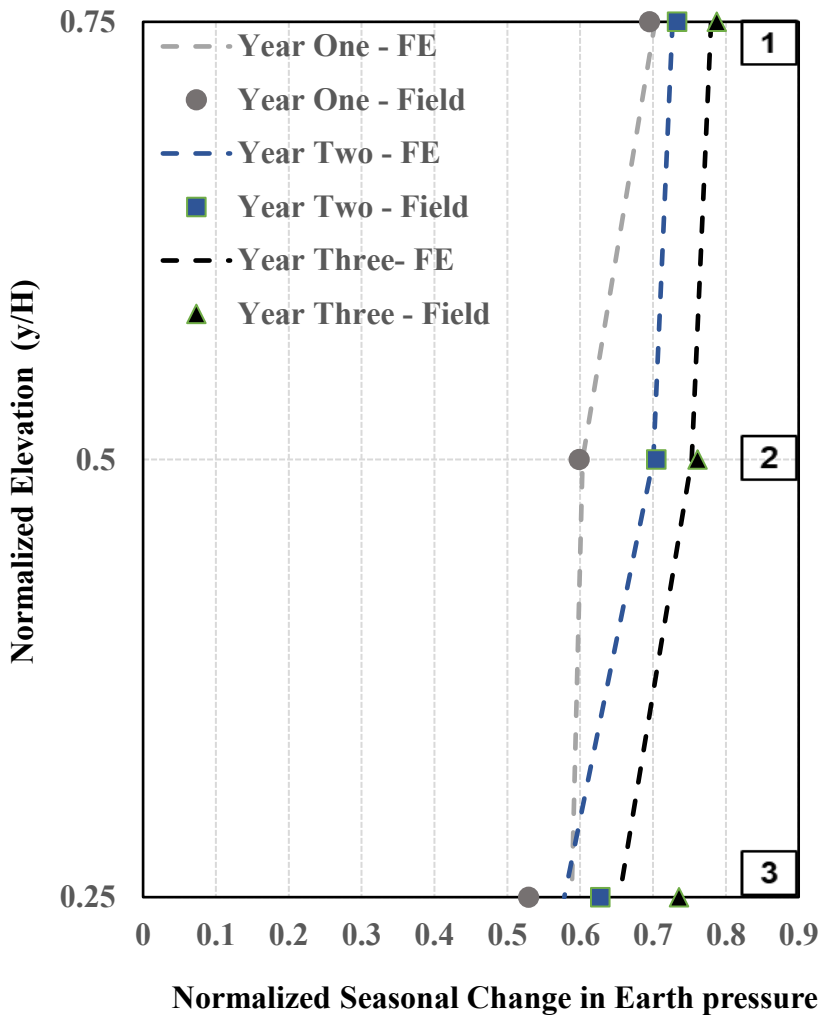

H= Total Height of abutment and Y= point depth

Figure 4.16: Comparing the observed Field earth pressure and the FE-model results using the Hardening Soil Model.

Figure 4.17 indicates that the maximum error value (%) in estimating the Hardening Soil FE-Model's earth pressure is 11.2%, which appears due to the first cyclic displacement at the third point (at elevation +15.74). However, the maximum error (%) value in points 1 and 2 is 1.1%.

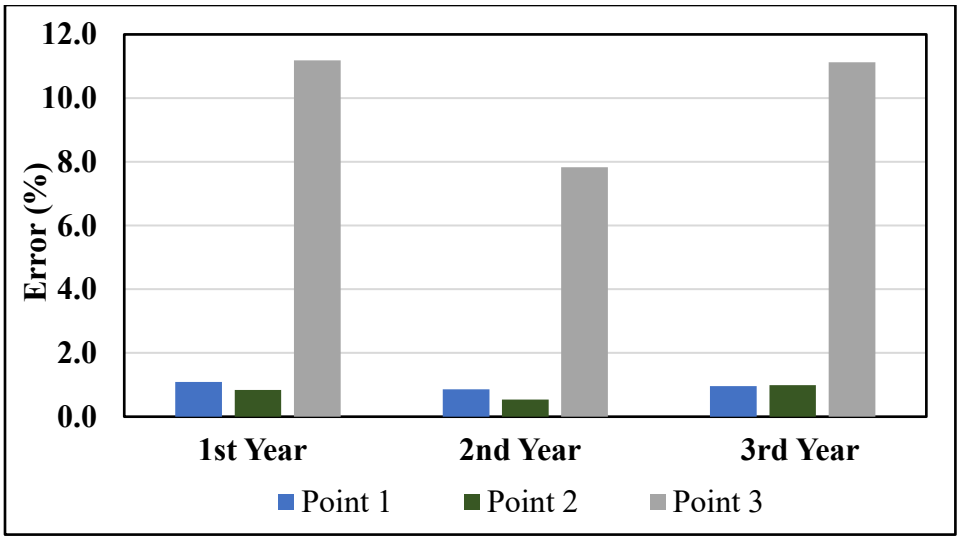

Figure 4.17: The error (%) in estimating earth pressure in the first F.E. Model using the Hardening Soil model.

4.7 Conclusion

At the end of each analysis, it is evident that the Mohr-Coulomb soil model cannot simulate the backfill materials' behaviour due to its constant stiffness theory. That said, the Hardening Soil model's accountability for the stress-dependent variation of stiffness successfully made it suitable to simulate the non-linear behaviour of the backfill soil.

CHAPTER FIVE

INVESTIGATION OF THE VIABILITY OF VARIOUS BACKFILLING OPTIONS

5.1 Introduction

Every backfill material possesses a property known as Lateral earth pressure as discussed in previous chapters. This lateral earth pressure mainly ranges from at-rest to active or at-rest to passive conditions, based on the structure's displacement. Consequently, the thermally influenced expansion of the deck of integral bridges causes the abutments to push against the backfill soil, leading to passive pressure from the backfill media. On the other hand, active pressure is exerted from the backfill soil when the abutment pulls away from the backfill media, as seen in Figure 5.1 (Thevaneyan et al., 2014). The magnitude of lateral earth pressure significantly alters the behaviour of structural elements (Arsoy et al., 2004). Consequently, it is essential to predict the performance of backfill materials before adopting them for integral bridges.

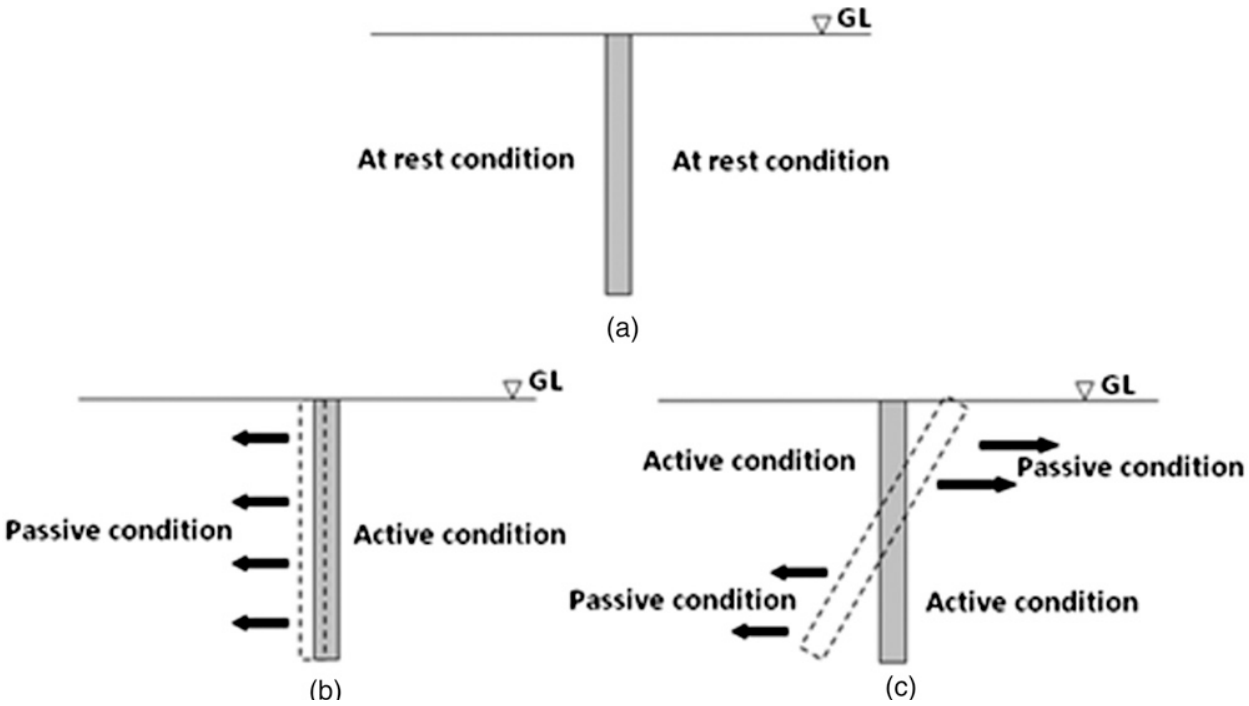

Figure 5.1: Schematic representations of earth pressure conditions influenced by structure's movement (Thevaneyan et al., 2014).

5.2 Parametric Case Study and Material Properties

The magnitude of earth pressure (active and passive) from different backfill options, including the field drainage material, was estimated using the hardening soil F.E. model validated in chapter four. These investigated backfill materials are Tire-Derived Aggregates (TDA), Expanded Polystyrene (EPS) Geofoam, Lightweight Expanded Clay Aggregate, EPS Composite Soil, Pit-run Gravel, Gravel A1 and Crushed Stone. Of these materials, only the EPS was analyzed using a linear-elastic model due to its material properties.

Table 5.1a and 5.1b below show the drainage materials properties investigated, using the hardening soil and linear-elastic models, respectively.

Table 5.1a: The drainage materials parameters analyzed using the hardening soil model.

Drainage Material	Ø°	C (Kpa)	E_{50} (Mpa)	E_{oed} (Mpa)	E_{ur} (Mpa)	ɣ (K.N./m^3)
TDA	26.5	24	4.50	3.6	13.5	7
Lightweight Expanded clay aggregate	38	5	6.8	5.4	20.4	4
EPS composite soil	25	250	20	16	60	10.5
Borrow A (Control Case)	34	29	40	32	120	21.7
Pit-run Gravel	31	0	35	28	105	18
Gravel A1	44	0	110	88	330	21
Crushed Stone	50	0	200	153	600	24

Table 5.1b: The drainage material parameters analyzed using the linear-elastic model.

Drainage Material	E (Kpa)	ɣ (K.N./m^3)	Ø°	ν
Expanded Polystyrene (EPS) Geofoam	6910	0.22	32	0.12

Necessary changes were made to the geometric layout and loading conditions of investigated materials to attain satisfactory results from the parametric research. A total of forty-three finite element analyses were conducted for this research, and the following changes were made before the analyses (Figure 5.2);

- A 10mm cycling displacement was introduced to replace the top transition sensor's field cycling displacements.
- The bottom cycling displacements were factored in by the new top cycling displacement and the field displacements.
- The drainage materials were modelled at different width values. B = 1m, 2m, 3m, 4m, 6m and 10m.

Other finite element conditions, material properties and construction procedures were kept constant as in the previous chapter. A sequence of how the drainage materials are subjected to the new cyclic displacements is shown in Table 5.2 below.

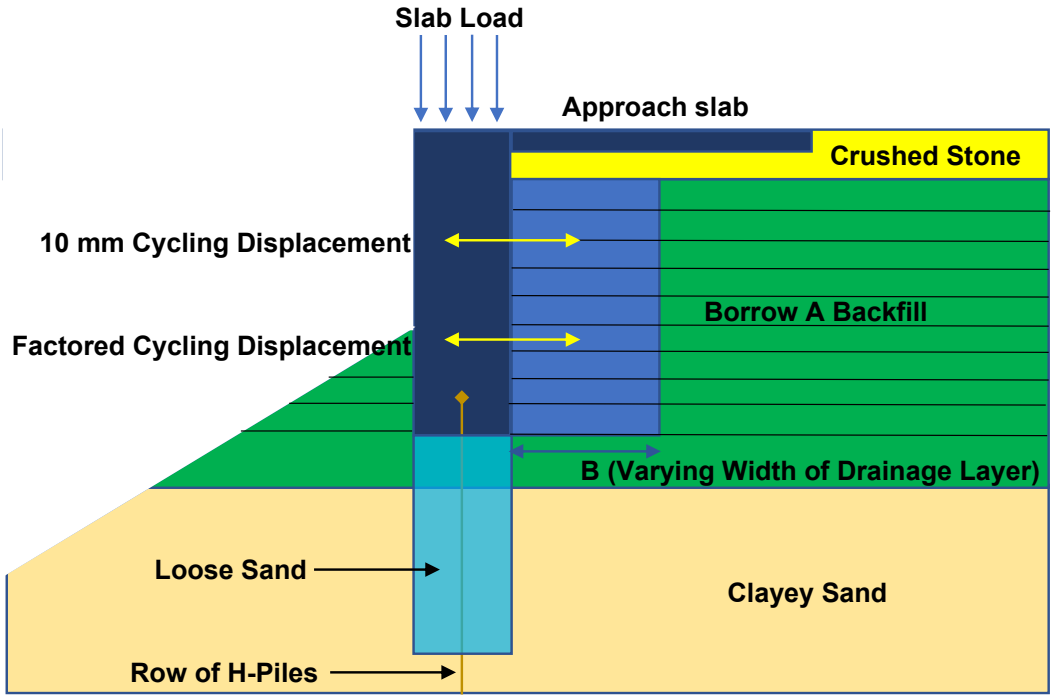

Figure 5.2: Finite-element alterations used for the parametric analyses.

Table 5.2: Increased cyclic displacements used for the parametric analyses.

Time	Displacement (mm)		Displacement Direction
	Upper sensor	Lower sensor	
Jan. 2005	10.0	9.5	Away from the backfilling
July. 2005	10.0	7.6	Towards the backfilling
Feb. 2006	10.0	7.9	Away from the backfilling
July. 2006	10.0	9.1	Towards the backfilling
Feb. 2007	10.0	11.3	Away from the backfilling
July. 2007	10.0	6.5	Towards the backfilling

5.3 Research Results and Interpretation

5.3.1 Total Lateral Thrust (T)

The total lateral thrust acting on the abutment is computed by integrating the lateral earth pressure acting on the total depth of the abutment. All the FE models follow the K_o procedure from its initial in-situ state; therefore, the total lateral thrust is calculated as:

$$T = \int_0^{H_{abut}} \sigma_h \, dz \qquad (5.3.1.1)$$

Where;

T is the total lateral thrust acting on the abutment.

H_{abut} is the height of the abutment.

σ_h is the lateral earth pressure acting on the abutment.

5.3.2 Isolation Efficiency (I.E.)

Isolation efficiency (IE) is a standard approach to assess the performance of one material in comparison to another; thus, it can be used in the case of soil materials. It can be defined as the difference between the total lateral thrust by the control material and another backfill material divided by the control material's total lateral thrust. The higher the isolation efficiency of backfill material, the higher its performance and vice versa.

The mathematical formula for Isolation Efficiency is expressed as follows;

$$IE = \frac{(T_o - T_{Inclusion})}{T_o} \times 100 \qquad (5.3.2.1)$$

Where;

T_o is the total lateral thrust on the abutment by the control material.

$T_{Inclusion}$ is the total lateral thrust on the abutment by an investigated backfill material.

5.3.2.1 Isolation Efficiency Results During The Active Mode

As stated earlier, all the drainage backfill materials were analyzed for different widths to know the magnitude of pressure/thrust generated behind the abutment. Figure 5.3 below clearly shows the three-year winter isolation efficiency comparison of the drainage backfill materials due to these lateral thrusts at different width values. In general, it is observed that an increase in the width of the drainage layers leads to a decrease in isolation efficiency during the active mode till stability is maintained.

For the three years, the 1m to 3m drainage layer widths of the heavy materials showed a linear reduction in performance before stabilizing to 10m. Also, the Pit-run gravel exhibits lower efficiency than the Gravel A1 and Crushed stone due to its less stiffness property and friction angle resulting in less shearing resistance during unloading. On the other hand, the light drainage materials showed a linear decrease in efficiency from 1m to 6m width, where stability occurred till 10m width. Only the EPS composite soil showed slight stability in performance with a minimum efficiency of 20.9% and a maximum efficiency of 100%. It is also the best performing material under unloading conditions for most width cases during the active mode.

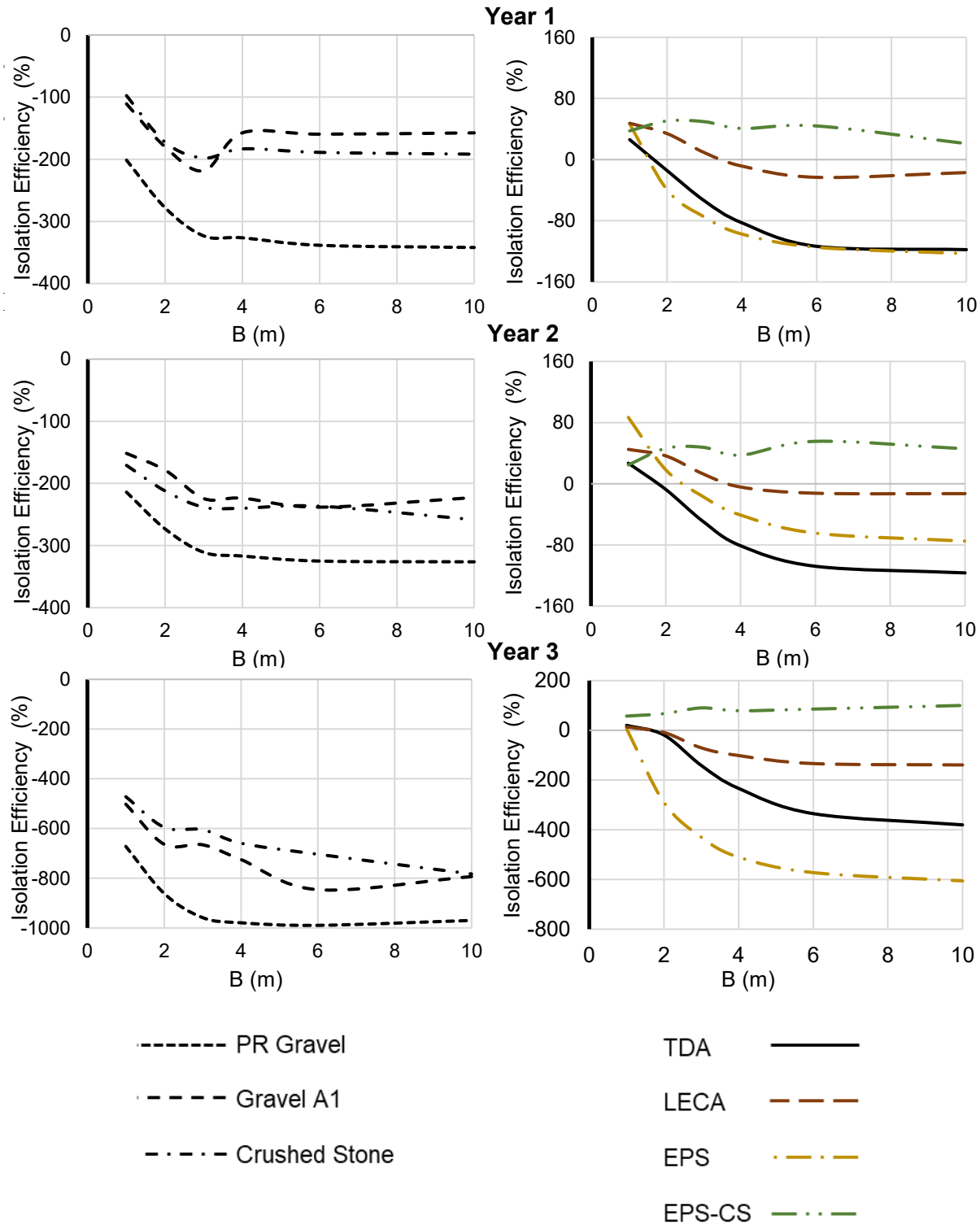

Figure 5.3: Isolation efficiency of the drainage materials based on active pressure distribution.

5.3.2.2 Isolation Efficiency Results During The Passive Mode

Figure 5.3 below indicates the three-year summer isolation efficiency comparison of the drainage backfill materials due to lateral thrusts at different width values. Overall, most of the materials showed consistent isolation efficiency at most drainage widths during the passive mode.

The Pit-run gravel shows a linear rise in efficiency amongst the heavy materials during the study period from 1m to 3m width before stabilizing to 10m. On the contrary, the Gravel A1 and Crushed stone indicate a continuous decrease in efficiency with the increasing width of the drainage layer for the three years. This result is due to additional drainage materials, which lead to more resistance during the passive mode. The light materials showed stable performance at most width points, with the Lightweight expanded clay aggregate, TDA and Expanded Polystyrene showing peak efficiency at 3m width during the study duration. Conversely, the EPS composite soil indicates lower efficiency than the lighter materials due to its resistance to loading, which can be attributed to its higher cohesive strength, friction angle and stiffness properties.

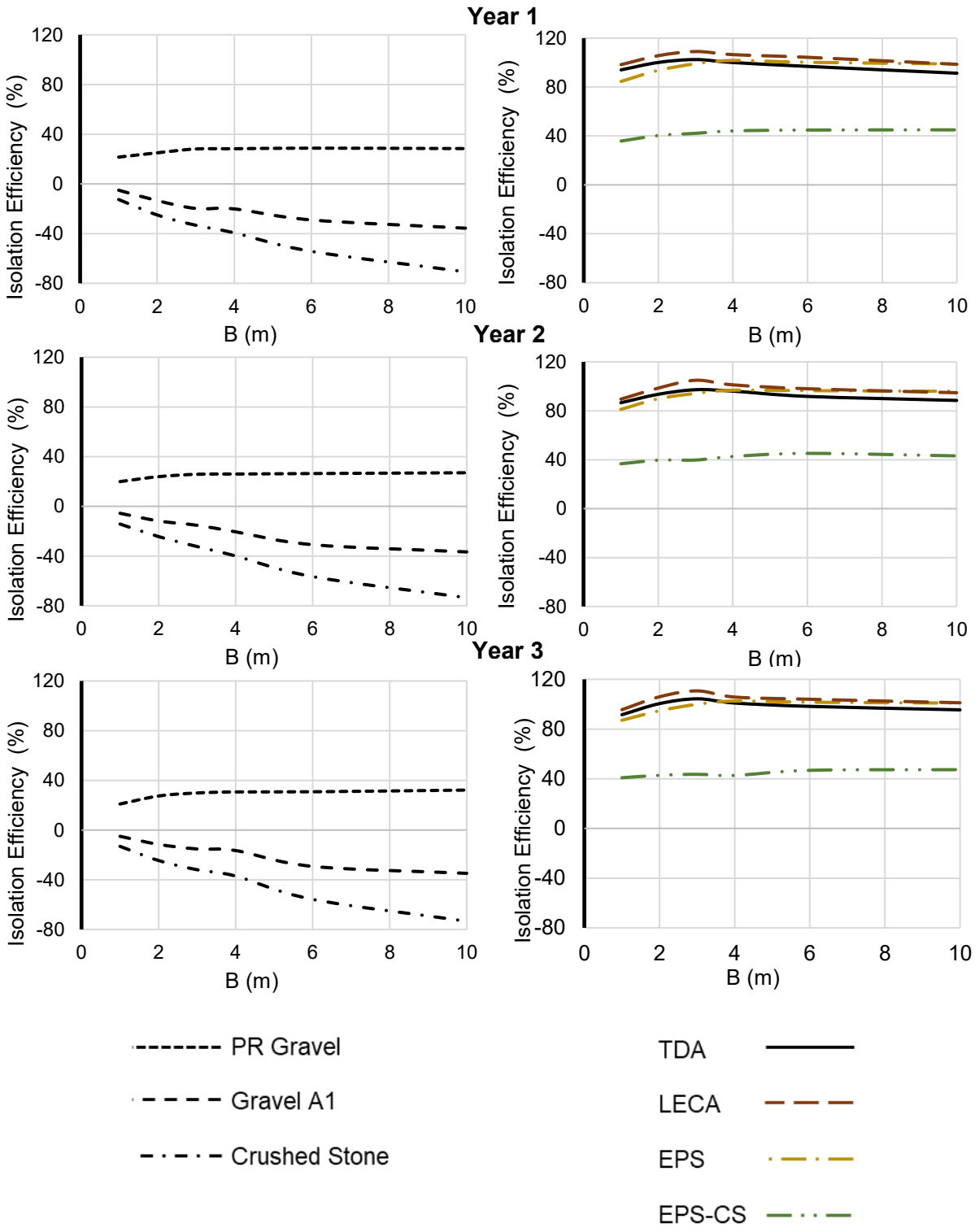

Figure 5.4: Isolation efficiency of the drainage materials based on passive pressure distribution.

5.3.3 Rankine Lateral Earth Pressure Coefficients

The coefficient of lateral earth pressure, K, is defined as the ratio of the effective horizontal pressure to the effective vertical pressure in a given soil mass. A volume of soil placed naturally or by laboured efforts possesses an at-rest pressure coefficient, K_0, a median earth pressure coefficient between active and passive earth pressure coefficients, K_A and K_P. When the soil mass is laterally elongated to the point of minimal-horizontal pressure, K_0 reduces to K_A and the active Rankine state is reached. On the other hand, the continuous lateral compaction of the soil mass leads to a maximum value in horizontal pressure where K_0 rises to K_P and the passive Rankine state is attained (Terzaghi et al., 1996).

The following equations are used to estimate the Rankine coefficients of active and passive earth pressures, respectively.

$$K_A = \frac{\sigma'_h}{\sigma'_v} = tan^2\left(45 - \frac{\phi'}{2}\right) \quad (5.3.3.1)$$

and

$$K_P = \frac{\sigma'_h}{\sigma'_v} = tan^2\left(45 + \frac{\phi'}{2}\right) \quad (5.3.3.2)$$

Where, σ'_h is the effective horizontal stress, σ'_v is the effective vertical stress and ϕ' is the angle of internal friction (Terzaghi et al., 1996).

5.3.4 Lateral Earth Pressure Coefficient Ratio

In addition to Isolation efficiency, the total lateral thrusts estimated using the finite element analyses were also used to recalculate the coefficient of lateral earth pressure, K_{FE}. These finite element coefficients were subsequently normalized using the appropriate Rankine active and passive pressure coefficients during the winter and summer seasons. This idea is to see if the drainage materials will be within the Rankine upper and lower limits of plastic equilibrium with an increase in drainage width value. The normalized coefficient of lateral earth pressure $\frac{K_{FE}}{K_a \text{ or } K_p}$, is another reliable way of analyzing the performance of the drainage materials at different width cases.

The mathematical expression for the coefficient of lateral earth pressure based on finite element results is shown below

$$K_{FE} = \frac{2}{\gamma H^2} \int_0^{H_{abut}} \sigma_h \, dz \qquad (5.3.4.1)$$

Where γ is the unit weight of the soil.

5.3.4.1 Lateral Earth Pressure Coefficient Ratio Results During The Active Mode

An overview of Figure 5.5 shows that an increase in width of the drainage materials may lead to a corresponding increase in $\frac{K_{FE}}{K_a}$ values before stabilities can be attained. These increments indicate a reduction in performance and are dependent on several soil properties.

The heavy materials at 1m to 3m drainage layer widths demonstrate a linear decrease in performance with an increase in $\frac{K_{FE}}{K_a}$ ratios for the three years, before rough stability, occurred till the 10m width. Of these materials, only the Pit-run gravel stayed within the Rankine limits with a minimum ratio of 0.64 at 1m width and a maximum ratio of 0.98 at 10m width, imposing lower lateral earth pressure than the Rankine's active earth pressure. Apart from the EPS composite soil, other light drainage materials showed an increasing trend, with the majority of the drainage widths (2m and above) over the $\frac{K_{FE}}{K_a}$ ratio of 1. In contrast to all other drainage materials, the EPS composite soil exhibits the best performance at all width values with minimum and maximum ratios of 0 and 0.23, respectively, satisfying Rankine theory.

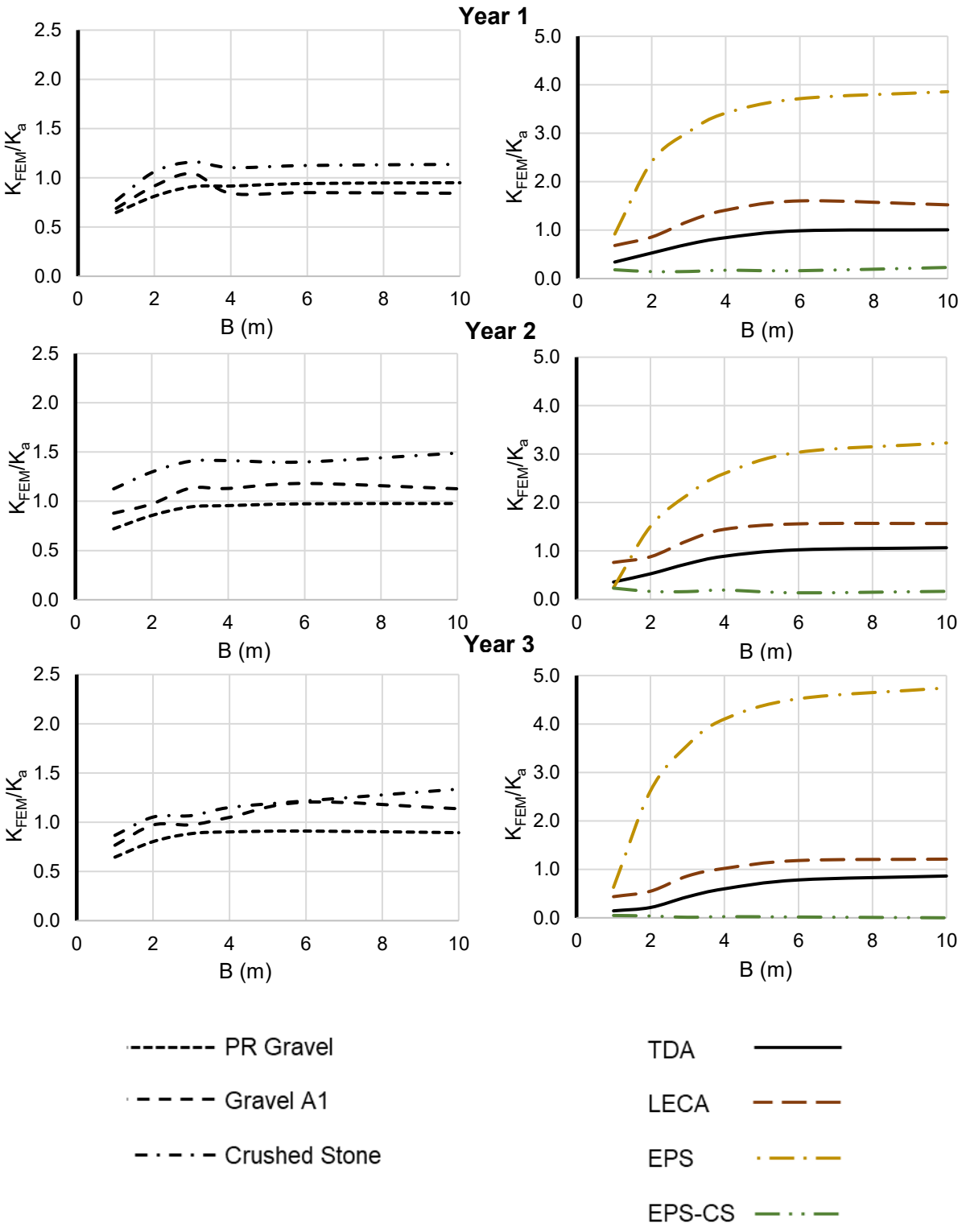

Figure 5.5: Lateral Earth Pressure Coefficient Ratio of the drainage materials based on active pressure distribution.

5.3.4.2 Lateral Earth Pressure Coefficient Ratio Results During The Passive Mode

In Figure 5.6, it is clear that all the heavy drainage materials are well within the Rankine passive pressure limit with a maximum $\frac{K_{FE}}{K_p}$ ratio of 0.74 at 1m width exhibited by the Pit-run gravel. The Crushed stone indicates better performance with a minimum $\frac{K_{FE}}{K_a}$ ratio of 0.25 at 1m width and a maximum value of 0.51 at 10m width for the study period. This three-year result shows that the higher the shear resistance of soil material, the lower its $\frac{K_{FE}}{K_p}$ ratio, meaning that more loading is required before shear failure can occur. Unlike other materials, the Geofoam showed a reducing trend in $\frac{K_{FE}}{K_p}$ ratio, giving its best performance at 4m and its worst performance at 1m over the three years. Other light materials remain slightly stable across the width values, as only the TDA and Lightweight expanded clay aggregate stayed within the Rankine limit of passive pressure $\left(\frac{K_{FE}}{K_p} < 1\right)$.

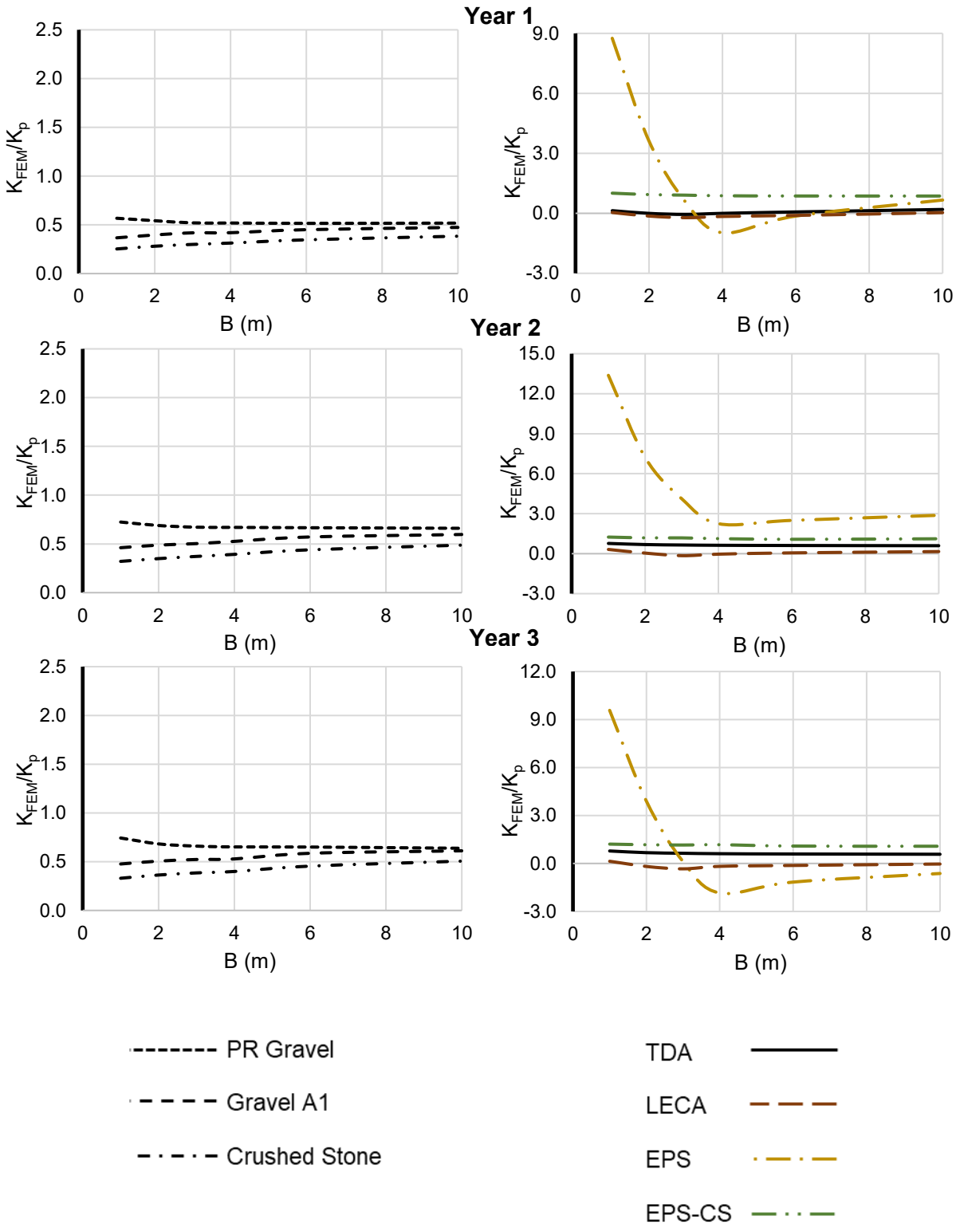

Figure 5.6: Lateral Earth Pressure Coefficient Ratio of the drainage materials based on passive pressure distribution.

5.3.5 Ground Level Settlement

Ground settlement or subsidence is a common problem in geotechnical engineering, and it is a vital consideration in the design of integral bridges. The continuous cyclic movement of the abutment causes the backfill material to subside, thereby creating a void right at the end of the bridge deck. According to Briaud et al., 1997, it is a consistent problem that can be limited through the use of well-compacted/stabilized fills, good fill material, approach slabs, sustainable drainage, to mention a few. Consequently, it is crucial to also analyze each drainage material by their respective ground level settlement from the F.E results.

5.3.5.1 Settlement Results During The Winter Seasons

Results shown in Figure 5.7 proves that all backfill materials will experience an increase in settlement with time, irrespective of the drainage layer width. The three heavy materials show a similar reducing trend in settlement, with the least settlement occurring at the 10m width for the three years. This reduction in settlement can be attributed to the addition of more drainage materials providing a better platform to resist sliding wedges at the top region of the backfill. The average minimum settlement of the heavy drainage materials is -13.49mm at 10m width during the first year, and the average maximum settlement is -36.65mm at 1m width during the third year. The TDA and the Lightweight expanded clay aggregate showed an opposite trend in settlement, with the most vertical displacement occurring at the 10m width. Compared to other drainage materials, the linear elastic geofoam is the best performing material with a minimum settlement of -10.45mm at 6m width and a maximum settlement of -17.55mm at 2m width over the years.

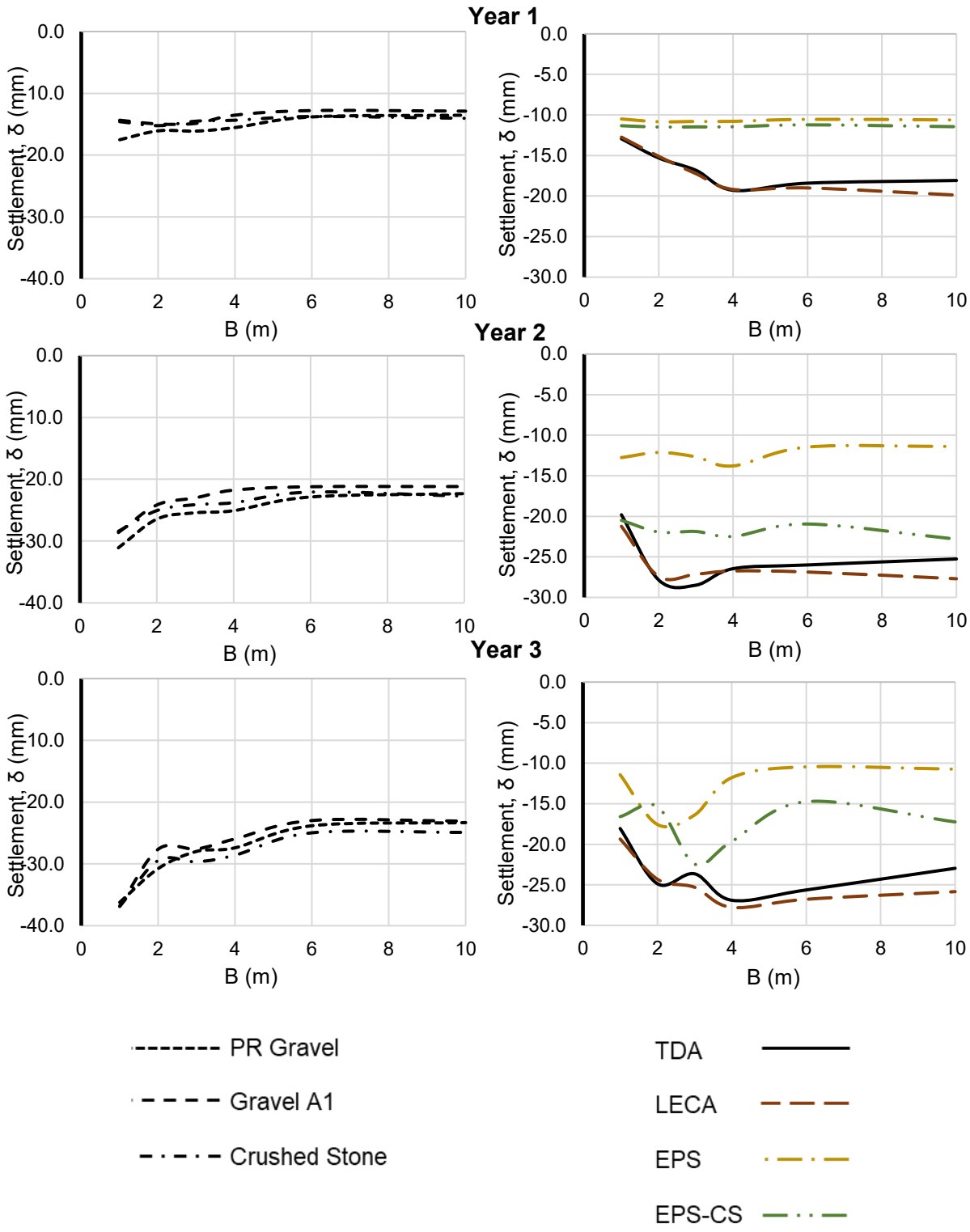

Figure 5.7: Ground level settlement results based on winter abutment displacements.

5.3.5.2 Settlement Results During The Summer Seasons

As seen in Figure 5.8, the summer abutment displacement causes similar trends in backfill settlement as those in Figure 5.7 over the three years. Contrary to the winter results, The heavy drainage materials showed lower average minimum and maximum settlements of -11.31mm and -19.22mm, respectively, for the study period. The TDA and LECA showed the highest settlements at 10m width, just as the active case but with lesser values. On the other hand, the geofoam maintains its overall best performance with improved minimum and maximum settlements of -6.99mm and -11.55mm, respectively. This general reduction in settlements from passive conditions can be referenced to the direction of sliding wedges during loading (upwards) instead of the downward movement which occurs during active conditions.

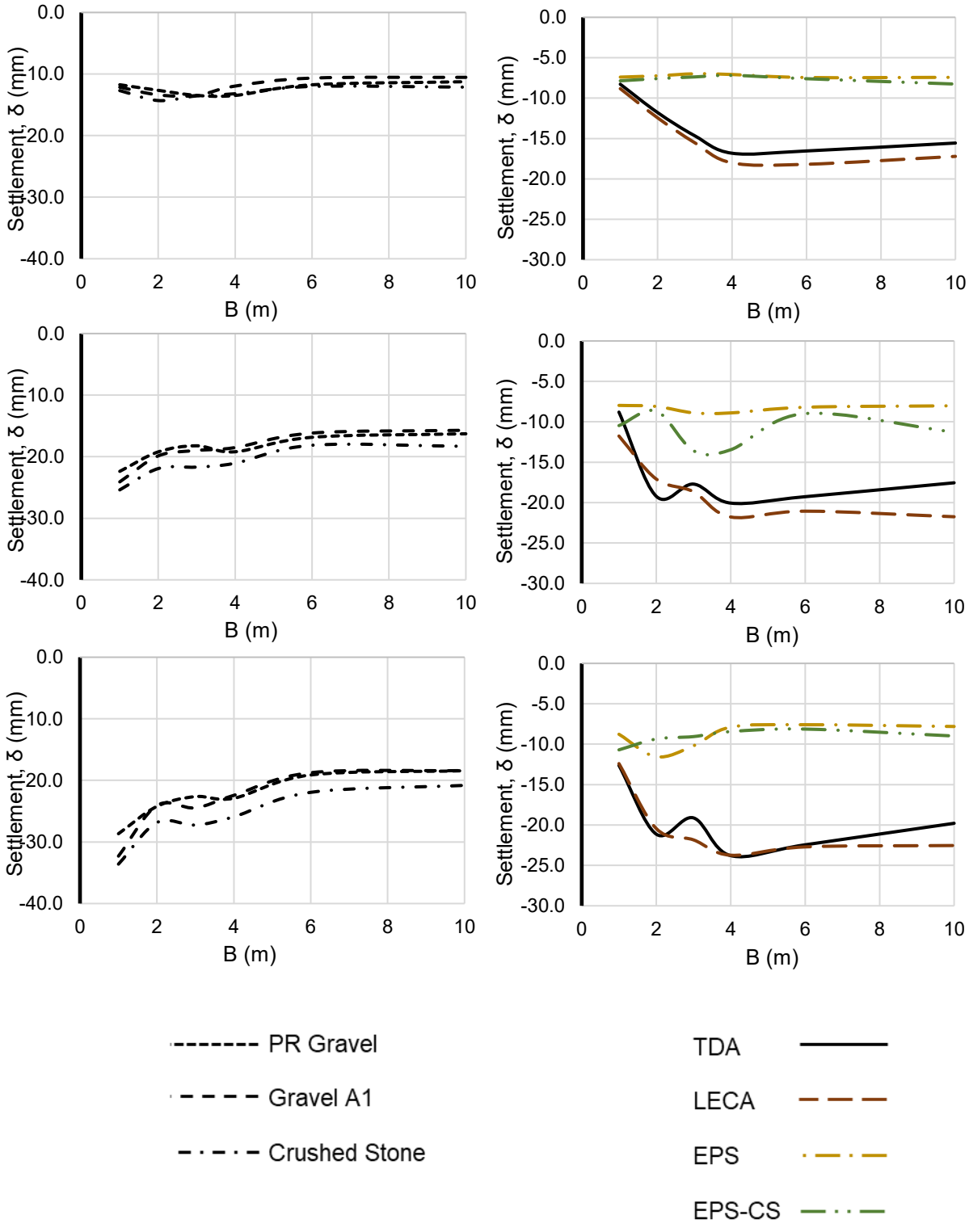

Figure 5.8: Ground level settlement results based on summer abutment displacements.

5.3.6 Long-term Performance of The Most Efficient Drainage Materials

Figure 5.4 in section 5.3.2.2 shows the most critical isolation efficiency from the backfill materials, of which the TDA, LECA and EPS gave their best performance at approximately 3m widths. For this reason, long-term analyses were conducted on these materials and compared to the long-term efficiency of the Pit-run gravel (Field drainage material).

As seen in Figure 5.9 below, the investigated drainage materials were subjected to a total of 90 cycles to know their minimum possible efficiencies under passive conditions. This reduction in efficiency indicates an increase in total lateral thrust from each drainage backfill, and its maximum steady value is vital for the design and behaviour of integral bridge abutments. The least-performing pit-run gravel shows its minimum stable average isolation efficiency of 20% after 66 cycles, implying an average maximum lateral thrust of 439KN. However, Significant improvements are indicated by the TDA and LECA with minimum efficiencies of 84.7% and 87.9%, respectively, after 83 cycles. These results also imply that the TDA imposes a constant maximum lateral thrust of 102KN while the LECA exerts a lower value of 81KN. Of all the materials, only the EPS Geofoam shows a different trend, with the minimum efficiency of 89.8% occurring between cycles 38 and 44, exerting a maximum lateral thrust of 68KN followed by an increase in efficiency till the 90th cycle. This unique best-performing property can be attributed to the linear-elastic theory followed by geofoam materials.

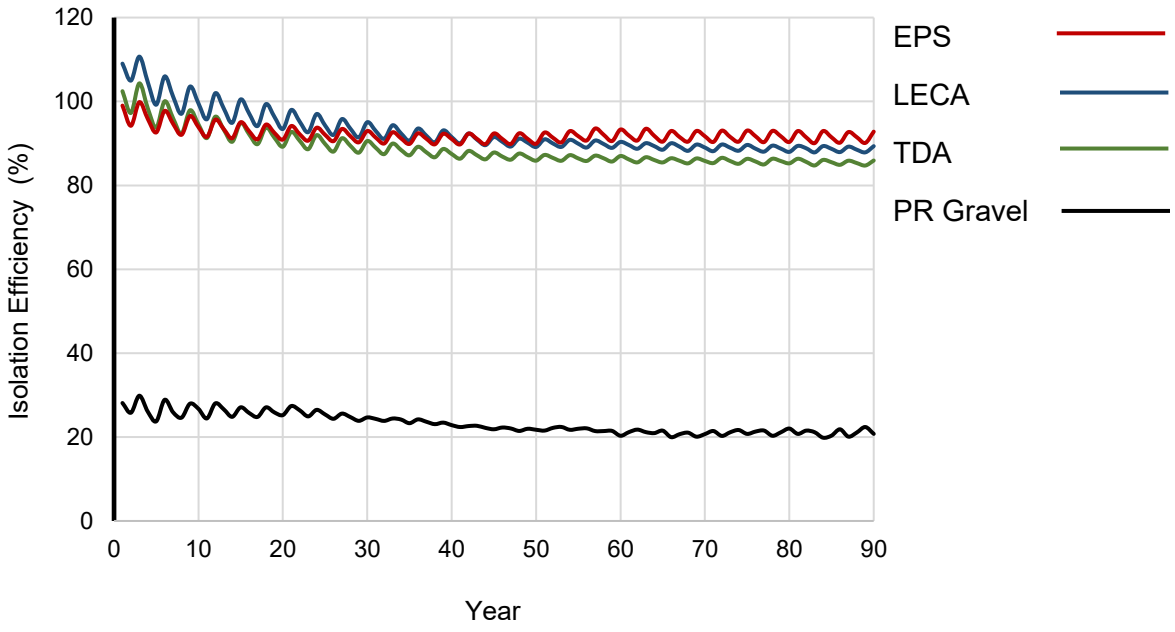

Figure 5.9: Comparison between the long-term performance of the most efficient drainage materials and the field drainage backfill.

CHAPTER SIX

CONCLUSIONS

6.1 Research Summary and Conclusions

In this research, intensive reviews were first conducted on diverse works of literature to acknowledge and spot research gaps related to integral abutment bridges. The east abutment soil-structure interaction of the Industrial Park-Route 2 Integral Bridge located in New-Brunswick was considered for investigation using the Mohr-Coulomb and Hardening Soil models on PLAXIS 2D. These analyses follow the same geometry, layout and construction procedure of the full-scale integral bridge to mimic how the backfill soil and abutment relate and to authenticate the numerical results. Results of these finite element analyses proved that only the hardening soil can simulate the non-linear behaviour of the backfill materials.

With the validated hardening soil model, further analyses were conducted on the performance of different backfill alternatives under three essential criteria; Isolation efficiency, Lateral earth pressure coefficient ratio and Ground-level settlement. The cyclic displacements of the east abutment modelled in chapter four of this study were increased to analyze the backfill materials under critical thermal conditions. Also, each backfill material was analyzed at different drainage widths to see the effect on their performance. A total of seven backfill materials; TDA, Expanded polystyrene (EPS) Geofoam, Lightweight Expanded clay aggregate, EPS composite soil, Pit-run gravel, Gravel A1 and Crushed Stone, were investigated in this research. Of all the investigated drainage materials, only the Geofoam was analyzed using the linear-elastic model.

The conclusions deduced from this research are stated as follows:

- The low efficiency portrayed by the EPS composite soil, Pit-run Gravel, Gravel A1 and Crushed stone during passive conditions makes them less suitable for integral bridges. That is, the adoption of these materials will require more design and maintenance costs of integral bridge abutments.

- Long-term performances showed by the Lightweight Expanded clay aggregate, and Expanded polystyrene (EPS) Geofoam at 3m width suggest their suitability although, their lateral earth pressure coefficient ratio during active conditions might be a concern.

- Of all the investigated backfill materials, only the Tire Derived Aggregate (TDA) at 3m width stayed within the Rankine active and passive limits of plastic equilibrium, maintaining peak isolation efficiency. Its long-term performance also indicates an acceptable minimum efficiency making it the most suitable drainage alternative for integral bridges.

- Overall, it is proven from this research that the stiffness of backfill materials should be their primary selection criterion for integral bridges. This parameter has a notable effect on pressure distribution; consequently, the long-term behaviour of these structures.

References

Alampalli, S. and Yannotti, A.P., 1998. In-service performance of integral bridges and jointless decks. *Transportation research record*, *1624*(1), pp.1-7.

American Association of State Highway and Transportation Officials. 2007. AASHTO American Association of State Highway and Transportation Officials, Washington, D.C.

Arockiasamy, M. and Sivakumar, M., 2005. Time-dependent behavior of continuous composite integral abutment bridges. Practice Periodical on Structural Design and Construction, 10(3), pp.161-170.

Arockiasamy, M., Butrieng, N. and Sivakumar, M., 2004. State-of-the-art of integral abutment bridges: design and practice. *Journal of Bridge Engineering*, *9*(5), pp.497-506.

Arsoy, S., 2000. Experimental and Analytical Investigations of Piles and Abutments of Integral abutment bridges (Doctoral dissertation, Doctoral Thesis, Blackburg, Virginia Polytechnic Institute and State University).

Arsoy, S., Barker, R.M. and Duncan, J.M., 1999. The behavior of integral abutment bridges.

Barker, K.J. and Carder, D.R., 2001. Performance of an integral bridge over the M1-A1 link road at Branham Crossroads. *TRL REPORT 521*.

Briaud, J.L., 1997. *Settlement of bridge approaches* (Vol. 234). Transportation Research Board.

Burke Jr, M.P., 2009. Integral and semi-integral bridges. John Wiley & Sons.

Canadian Standards Association. 2006. CAN/CSA-S6-06: Canadian highway bridge

Chang, L.M. and Lee, Y.J., 2002. Evaluation of performance of bridge deck expansion joints. Journal of performance of constructed facilities, 16(1), pp.3-9.

Clayton, C.R.I., Xu, M. and Bloodworth, A., 2006. A laboratory study of the development of earth pressure behind integral bridge abutments. *Géotechnique*, *56*(8), pp.561-571.

Comisu, C.C. and Gheorghita, B., 2010. Integral bridges and environmental conditions. In *Proceedings of the International Conference on Risk Management, Assessment and Mitigation* (pp. 164-169).

Darley, P. and ALDERMAN, G., 1995. Measurement of thermal cyclic movements on two portal frame bridges on the M1. *TRL Report*, (165).

Darley, P., Carder, D.R., and Barker, K.J. 1998. Seasonal thermal effects over three years on the shallow abutment of an integral bridge in Glasgow. *Transportation Research Laboratory Report* 344, Transportation Research Laboratory, Wokingham, Berkshire, UK.

David, T.K., Forth, J.P. and Ye, J., 2014. Superstructure behaviour of a stub-type integral abutment bridge. *Journal of Bridge Engineering*, *19*(6), p.04014012.
design code. 2nd ed. Canadian Standards Association, Mississauga, O.N.

Duncan, J.M. and Arsoy, S., 2003. Effect of bridge-soil interaction on the behaviour of piles supporting integral bridges. *Transportation research record*, *1849*(1), pp.91-97.

England, G.L. and Tsang, N.C.M., 2001. Towards the design of soil loading for integral bridges-experimental evaluation. *Department of Civil and Environmental Engineering, Imperial College, London*.

Faraji, S., Ting, J.M., Crovo, D.S. and Ernst, H., 2001. Nonlinear analysis of integral bridges: finite-element model. Journal of Geotechnical and Geoenvironmental Engineering, 127(5), pp.454-461.

Fennema, J.L., Laman, J.A. and Linzell, D.G., 2005. Predicted and measured the response of an integral abutment bridge. *Journal of Bridge Engineering*, *10*(6), pp.666-677.

Frosch, R.J., Wenning, M., and Chovichien, V. 2005. The in-service behaviour of integral abutment bridges: Abutment-pile response. *In* Proceedings of the FHWA Conference on Integral Abutment and Jointless Bridges, Baltimore, Maryland, 16-18 March 2005. Federal Highway Administration, Washington, D.C., pp. 30-40.

GangaRao, H., Thippeswamy, H., Dickson, B. and Franco, J., 1996, November. Survey and design of integral abutment bridges. In Workshop on Integral abutment bridges, November 13-15, 1996, Pittsburgh, PA (p. 129).

Girton, D.D., Hawkinson, T.R. and Greimann, L.F., 1991. Validation of design recommendations for integral-abutment piles. *Journal of Structural Engineering*, *117*(7), pp.2117-2134.

Hambly, E.C., 1997, February. INTEGRAL BRIDGES. In *Proceedings of the Institution of Civil Engineers-Transport* (Vol. 123, No. 1, pp. 30-38). Thomas Telford-ICE Virtual Library.

Hong, J.H., Jung, J.H., You, S.K. and Yoon, S.J., 2003. A simplified numerical model for an integral abutment bridge considering the restraining effects due to backfill. Journal of the Korea Concrete Institute, 15(5), pp.759-767.

Hoppe, E.J. and Gomez, J., 1996. Field study of an integral backwall bridge (No. VTRC 97-R7). Virginia Transportation Research Council.

Horvath, J.S., 2000. Integral-abutment bridges: problems and innovative solutions using EPS geofoam and other geosynthetics. Res. Rpt. No. CE/GE-00, 2.

Huang, J., Shield, C.K., and French, C. 2005. Time-dependent behaviour of a concrete integral abutment bridge. *In Proceedings of the 6th International Bridge Engineering Conference on Reliability, Security, and Sustainability in Bridge Engineering*, Boston, Massachusetts, 17-20 July 2005. Transportation Research Board, Washington, D.C., pp. 299-309.

Huntley, S.A., 2009. *Field Performance and Evaluation of an Integral Abutment Bridge* (Vol. 72, No. 08).

Husain, I. and Bagnariol, D., 2000. Design and performance of jointless bridges in Ontario: new technical and material concepts. *Transportation research record*, *1696*(1), pp.109-121.

Husain, I., Huh, B., Low, J., and McCormick, M. 2005. Moose Creek Bridge - A case study of a prefabricated integral abutment bridge in Canada. Proceedings of the FHWA Conference on Integral Abutment and Jointless Bridges, Baltimore, Maryland, 16-18 March 2005. Federal Highway Administration, Washington, D.C., pp. 148-160.

Jayaraman, R. and Merz, P.B., 2001, August. Integral bridge concept applied to rehabilitate an existing bridge and construct a dual-use bridge. In 26th Conference on our World in Concrete and Structures (pp. 26-28).

Kim, W. and Laman, J.A., 2012. Seven-year field monitoring of four integral abutment bridges. *Journal of Performance of Constructed Facilities*, *26*(1), pp.54-64.

Knickerbocker, D.J., Basu, P.K., Holloran, M.A. and Wasserman, E.P., 2003. Recent experience with high-performance concrete jointless bridges in Tennessee. *Transportation research record*, *1845*(1), pp.104-114.

Lawver, A., French, C. and Shield, C.K., 2000. Field performance of integral abutment bridge. Transportation Research Record, 1740(1), pp.108-117.

LRFD bridge design specifications 4th edition SI-units errata (LRFDSI-4-E5). 5th ed.

Maruri, R.F. and Petro, S.H., 2005. Integral abutments and jointless bridges (IAJB) 2004 survey summary. In *Integral Abutment and Jointless Bridges (IAJB 2005) Federal Highway AdministrationWest Virginia Department of Transportation*.

Mistry, V.C., 2005. Integral abutment and jointless bridges. In Integral Abutment and Jointless Bridges (IAJB 2005) Federal Highway Administration West Virginia Department of Transportation.

NBDTI. 2015. Standard specifications. The New Brunswick Department of Transportation and infrastructure, Fredericton, N.B.

Ooi, P.S., Lin, X. and Hamada, H.S., 2010. Field behaviour of an integral abutment bridge supported on drilled shafts. *Journal of Bridge Engineering*, *15*(1), pp.4-18.

Ooi, P.S., Lin, X. and Hamada, H.S., 2010. Numerical study of an integral abutment bridge supported on drilled shafts. *Journal of Bridge Engineering*, *15*(1), pp.19-31.

Schanz, T., 1999. Formulation and verification of the Hardening-Soil Model. *RBJ Brinkgreve, Beyond 2000 in Computational Geotechnics*, pp.281-290.

Soltani, A.A. and Kukreti, A.R., 1992. Performance evaluation of integral abutment bridges. *Transportation research record*, (1371).

Terzaghi, K., Peck, R.B. and Mesri, G., 1996. *Soil mechanics in engineering practice*. John Wiley & Sons.

Thippeswamy, H.K. and Gangarao, H.V., 1995. Analysis of in-service jointless bridges. *Transportation Research Record*, (1476).

Van Lund, J.A. and Brecto, B.B., 1999. Jointless bridges and bridge deck joints in Washington State. *Transportation research record*, *1688*(1), pp.116-123.

Wood, D. and Nash, D., 2000. Earth pressures on an integral bridge abutment: a numerical case study. *Soils and foundations*, *40*(6), pp.23-38.